



UNIVERSITÀ
DI TRENTO

PHYSICS DEPARTMENT

BACHELOR'S DEGREE IN PHYSICS

Tracking particles in high-radiation space environments

Supervisor:
Francesco Maria Follega

Graduating Student:
Luca Di Turi

ACADEMIC YEAR: 2024/25

DATE OF THE FINAL EXAM: 15/09/2025

Abstract

The investigation of the nature, composition, as well as the spatial and temporal distribution of particles trapped in the geomagnetic field is an interesting topic at the intersection of particle physics and geophysics. Moreover, it allows us to explore the structure of the field that contains them, its origin, and the physical reasons and mechanisms behind the trapping phenomenon. This work explores the physics of trapped particles, and it provides an overview of the population of particle belts. Additionally, it includes a synthetic excursus on the detector used to reconstruct the incoming direction of charged particles. The work also discusses some of the tracking algorithms used in the field, especially in space missions. Among the missions devoted to the monitoring of charged particles in space, there is the China Seismo-Electromagnetic Satellite (CSES) missions. This scientific mission is presented, with a focus on its objectives and instrumentation, in particular the new HEPD-02 and its pixel tracker, the first tracker of this type to be used in a space mission. Different types of particle detectors are described, analyzing their advantages and disadvantages. Tracking reconstruction methods are discussed, and an application of selected ones in the case of a three-layer silicon detector, as the one in HEPD-02, is presented. The first method is a combinatorial approach, based on the χ^2 minimization across all combinations of hit points; the second is a Hough Transform-based algorithm. These two techniques are applied to reconstruct tracks in 3 dimensions, using a simulated dataset, resembling the detector condition in space, and their performances are evaluated. Results are discussed, and tracking accuracy and computational efficiency are evaluated in single track and multi-track events. This study supports the possibility of multi-particle tracking in high radiation environments like the South Atlantic Anomaly (SAA), where the trigger rates are expected to be of the order of 1 MHz, enabling a refined estimation of the charged particle flux for missions like the CSES one.

Ringraziamenti

Prima di iniziare con gli argomenti seri, volevo spendere due parole per ringraziare alcune delle persone che mi hanno permesso di arrivare fino a qui. La laurea di sicuro è un traguardo personale, di cui vado molto fiero, ma sarebbe sciocco e presuntuoso attribuire il merito di tutto questo solamente a me e all'impegno che ci ho messo. Per questo elaborato finale devo quasi tutto al mio relatore, grazie mille Francesco per avermi sopportato in questi mesi ed avermi aiutato e seguito costantemente. Grazie ai miei genitori, a mia nonna ed a tutta la mia famiglia, che mi hanno fatto sentire a casa, anche quando eravamo distanti. Grazie per l'opportunità di seguire l'università da fuori sede, grazie per avermi permesso di crescere seguendo la mia strada, quasi sempre. Grazie poi a tutti gli amici, vicini e lontani, di lunga data ed i più recenti. Grazie perchè mi fate sentire una persona speciale, anche nei momenti più grigi. Grazie di tutto l'amore che mi avete dato, spero di avervene restituito almeno un po'.

Contents

1	Introduction	4
1.1	Particles trapped in the geomagnetic field	4
1.2	The CSES mission	14
1.3	The new pixel tracker of the High Energy Particle Detector (HEPD-02) on board the CSES-02 satellite	17
1.4	State-of-the-art in trapped particle flux modelling	19
2	Track reconstruction methods	22
2.1	Tracking technologies and track reconstruction methods	22
2.2	Tracking Reconstruction Algorithms	26
2.2.1	Combinatorial Method	26
2.2.2	Hough Transform Method	28
2.3	Prospects in Tracking with Deep Learning Methods	30
3	Dataset and results	31
3.1	Pseudo-dataset generation	31
3.2	Results on simulated data	33

Chapter 1

Introduction

1.1 Particles trapped in the geomagnetic field

The presence of particles trapped in the geomagnetic field is closely linked to the structure of the magnetic field surrounding our planet. For this reason, it is important to introduce their spatial and temporal distributions and to study their origin.

Structure of the Magnetosphere

The movement of the materials inside the Earth's core generates a magnetic field (with a variable strength at the surface from $\simeq 10^{-4}$ to $10^{-5} T$, respectively at the equator and near the poles or the South Atlantic Anomaly). The *magnetosphere* is the region of space where the geomagnetic field dominates over other external fields. The Sun emits the solar wind, a plasma of ions and electrons moving radially outward from its surface. The portion of the solar wind directed toward Earth interacts with the geomagnetic field at supersonic speeds. This interaction causes the formation of a shockwave at $\simeq 2 R_e^1$, ahead of the geomagnetic barrier. The reduction in velocity due to this shockwave makes the plasma flow around the field, the shell-like region between the shock and the magnetic boundary is called the *magnetosheath*. The inner boundary of this region, known as the *magnetopause*, separates the solar plasma and magnetic fields from the ones produced by Earth. On the side of Earth opposite the Sun, the magnetic field is stretched downstream into two lobes: in the northern lobe, the field lines point toward Earth, while in the southern lobe they are directed away from Earth. This configuration requires currents flowing across the tail and along the surface of the magnetosphere, as shown in Fig. 1.1.

¹ R_e : the Earth's radius, 6.37×10^3 km

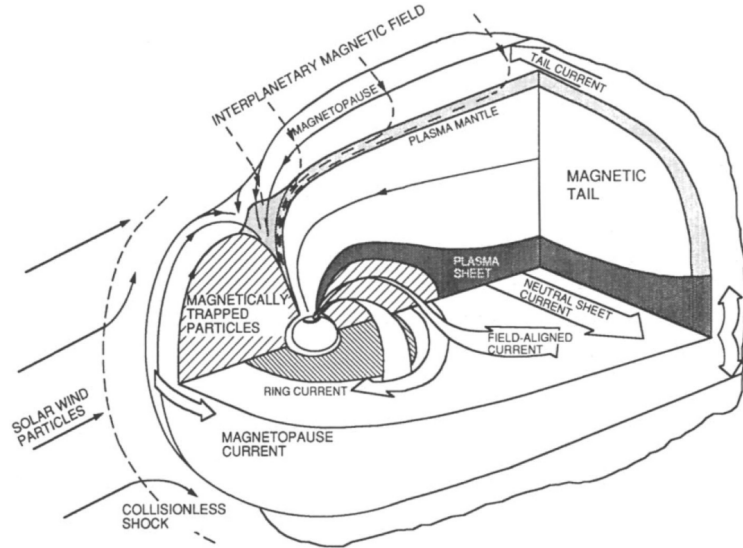


Figure 1.1: Visualization of the magnetic fields generated around Earth. The chart shows the different regions described in the main text (i.e., the magnetopause and tails). The action of the solar wind is displayed as well as the presence of the trapped particles and field currents arising in the interaction with the geomagnetic fields. [24], Fig. 1.1.

The separation between solar and geomagnetic fields is not strict: field lines from the two sources can merge, altering the behavior of the magnetosphere; furthermore, the system is not static: the solar wind is highly variable, and so is the structure of the tail. [24], Chap. 2.

The structure of the geomagnetic field

Many different current systems contribute to generate the geomagnetic field, but from the standpoint of a charged particle, the most effective is Earth's dynamo system. Inside Earth, hot conducting material is transported by convection, and this motion within the geomagnetic field induces currents that reinforce the field itself. Acting as a self-exciting dynamo, this process generates the main component of the geomagnetic field. This field remains steady on time scales shorter than a year, though geological evidence shows that it has reversed polarity at irregular intervals of about a million years.

The numerical value of the geomagnetic field can be obtained with a multipole expansion derived from stationary Maxwell's equations in the absence of currents. The lowest and dominant order of this expansion is the dipole term. Equation (1.1) describes the dipole potential, expressed in polar coordinates, where r is the distance measured from the center of the dipole, and θ is the polar angle (colatitude).

$$\psi(r) = R_E \left(\frac{R_E}{r} \right)^2 g_1^0 \cos\theta \quad (1.1)$$

The constant² g_1^0 is adjusted to fit experimental values of the magnetic field sampled on a

²In 1985, for a reference field, $g_1^0 = -29877$ nT (Reference Martin Walt p.28)

worldwide basis. The magnetic field \vec{B} is equal to $-\nabla\psi$:

$$B_r = -\frac{\partial\psi}{\partial r} = 2\left(\frac{R_E}{r}\right)^3 g_1^0 \cos\theta = -2B_0\left(\frac{R_E}{r}\right)^3 \cos\theta \quad (1.2)$$

$$B_\theta = -\frac{1}{r} \frac{\partial\psi}{\partial\theta} = \left(\frac{R_E}{r}\right)^3 g_1^0 \sin\theta = -B_0\left(\frac{R_E}{r}\right)^3 \sin\theta \quad (1.3)$$

where $B_0 = 3.12 \times 10^{-5}$ T is the mean value of the geomagnetic field at the equator on Earth's surface. The components are expressed in spherical coordinates, with a negative sign in the expressions containing B_0 because the field direction is opposite to the corresponding unit vectors. The ϕ component of B is absent since the potential does not depend on ϕ , and therefore $\partial\psi/\partial\phi = 0$. This implies that the predicted field lines are constant at a fixed value of θ (latitude). As shown in the Fig. 1.2, this symmetry is not perfectly realized in the actual field: although the dipolar nature is evident (with poles shifted relative to the geographic ones), deviations arise from additional contributions to the geomagnetic field, which can be treated separately. [24], Chap. 3.

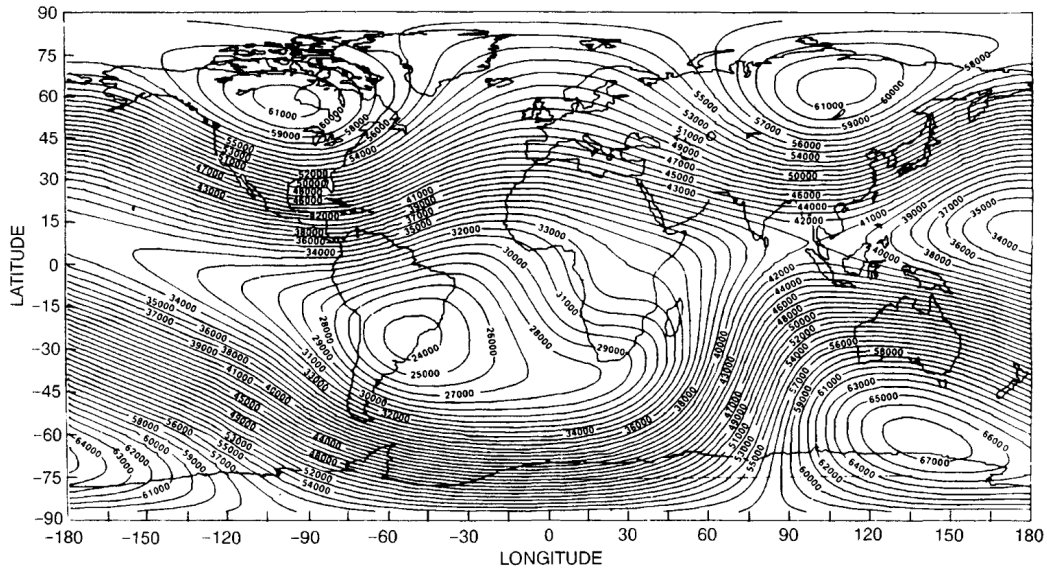


Figure 1.2: Visualization of the isointensity lines of the geomagnetic field at Earth's surface. The magnetic field is expressed in units of 10^{-9} T. The chart shows the deviations from the ideal dipole field, with the South Atlantic Anomaly clearly visible and the field lines appearing non-parallel at different latitudes. [24], Fig. 3.2.

The Radiation belts

The radiation belts, also known as *Van Allen* belts, are regions within the magnetosphere where energetic ions and electrons are trapped. Magnetic trapping requires relatively stable fields, and for this reason the belts extend from the end of the atmosphere at 200 - 1000 km to $\simeq 7 R_e$. Outside this range, solar-wind fluctuations prevent trapping, while at lower altitudes collisions between particles and atmospheric constituents produce similar effects.

The study of trapped particles around Earth is important because they can be measured with high precision, and a deep understanding of Earth's plasma environment may provide valuable insights into phenomena occurring at larger scales that cannot be directly observed. Although most of the magnetosphere has been explored, our knowledge decreases with increasing distance from Earth.

Moreover, the magnetically trapped ions pose serious problems for space crafts: sensors can be damaged by particle impacts, and their performance may degrade due to the noisy background generated by interactions in electrically active volumes. Furthermore, ions and electrons may deposit charge on the spacecraft surface, producing potential differences between segments; the subsequent discharge can damage onboard electronics and generate spurious signals. So, a deep understanding of the Van Allen belts can be used in future space missions to minimize such problems. [24], Chap. 1.

Why particles get trapped

To understand why and how particles are trapped inside the magnetosphere, it is important to understand their law of motion. The fundamental equation describing the motion of a charged particle in electro-magnetic fields is the Lorentz equation:

$$\vec{F} = \frac{d\vec{p}}{dt} = q \left(\vec{E} + \vec{v} \times \vec{B} \right) \quad (1.4)$$

where \vec{F} is the force acting on the particle, \vec{p} is its linear momentum, q is the electric charge, \vec{v} the velocity, and \vec{E} and \vec{B} the external electric and magnetic fields, respectively. In the case of simple geometries, the eq (1.4) can be analytically integrated to derive the ideal trajectory of the particle, but this procedure is impossible without assumptions on the geomagnetic field, and one must resort to approximations or numerical integration techniques. Radiation belt particles have such a low energy that in their frame of reference the magnetic field appears almost uniform; so, an efficient approximate theory has been developed to describe their motion. First of all, we note that equation (1.4) can be separated into components parallel and perpendicular to the magnetic field:

$$\left(\frac{d\vec{p}}{dt} \right)_\parallel = q \vec{E}_\parallel \quad \text{and} \quad \left(\frac{d\vec{p}}{dt} \right)_\perp = q \left(\vec{E}_\perp + \vec{v} \times \vec{B} \right) \quad (1.5)$$

, where the first equation describes the motion parallel to the magnetic field, while the second one describes the motion perpendicular to it.

Using this equation, we start by analyzing the motion of particles in simple geometries.

Motion of particles in a uniform magnetic field

Assuming uniform \vec{B} and null \vec{E} , the equations (1.5) become:

$$\left(\frac{d\vec{p}}{dt} \right)_\parallel = 0 \quad (1.6)$$

$$\left(\frac{d\vec{p}}{dt} \right)_\perp = q(\vec{v} \times \vec{B}) = q(\vec{v}_\perp \times \vec{B}) \quad (1.7)$$

from (1.6), we see that $(d\vec{p}/dt)_\parallel$ is constant, so the particle moves parallel to \vec{B} at a constant speed; from (1.7) we see that the momentum change is perpendicular to \vec{v}_\perp . Therefore, the trajectory is a circle of radius ρ when projected in a plane perpendicular to \vec{B} .

$\rho = p_\perp/Bq$ is called gyroradius or cyclotron radius, and the angular frequency of the gyration motion, the gyrofrequency is $\Omega = Bq/m$ [radians/s]; in the non-relativistic case (valid for particles in the radiation belts) it is independent of the particle's energy. In the case of a uniform magnetic field with no electric field, the charged particles describe an helix, with the circular motion perpendicular to \vec{B} . An important quantity to describe this motion is the pitch angle of the helix, defined as the angle between the particle velocity and \vec{B} : $\alpha = \tan^{-1}(v_\perp/v_\parallel)$, visible in the Fig. 1.3 .

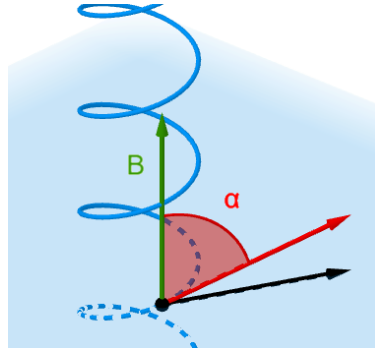


Figure 1.3: Visualization of the Pitch Angle α of a particle in helicoidal motion. α is the angle between the magnetic field \vec{B} , in green, and the particle's linear momentum, in red.

The helical motion is the primary motion of particles in the geomagnetic field, because the field's non-uniformities are small over distances the length of the gyroradius.

Motion of particles in a uniform magnetic and electric field

If \vec{E}_\parallel is constant, the particle gets uniformly accelerated, following the equation $\vec{p}_\parallel(t) = \vec{p}_\parallel(0) + q\vec{E}_\parallel t$. This leads to a deformed gyromotion, drifting at velocity $\vec{v}_E = (\vec{E} \times \vec{B})/B^2$, perpendicular to \vec{E} and \vec{B} , as described in Fig. 1.4. All charged particles drift in the $\vec{E} \times \vec{B}$ direction, with a velocity independent of the particle's charge, mass, or velocity.

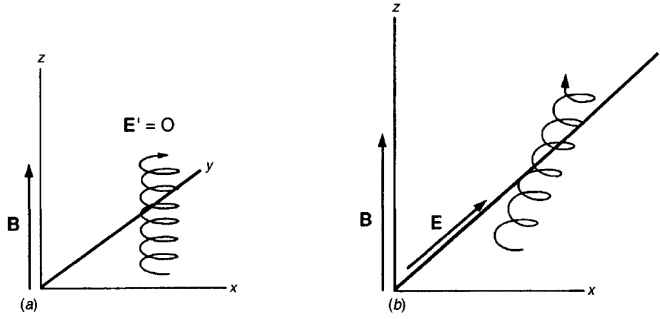


Figure 1.4: Visualization of the gyration motion of a charged particle. On the left: case with $\vec{B} \neq 0$ and $\vec{E}' = 0$, showing a helical trajectory. On the right: case with $\vec{B}, \vec{E} \neq 0$ and $\vec{B} \perp \vec{E}$, showing an additional drift in the $\vec{E} \times \vec{B}$ direction. [24], Fig. 2.1.

Motion of particles in an inhomogeneous magnetic field

To address the case of an inhomogeneous magnetic field, we note that even for trapped electrons and protons with energies of several MeV, $R_e \gg \rho$, and the geomagnetic field experienced by a particle during a single gyration can be considered almost uniform. This allows us to perform a Taylor expansion of the magnetic field about the particle's position. Small deviations from ideal helical motion, induced by the gradient $\nabla \vec{B}$, accumulate over time and lead to significant deviations from the reference trajectory.

Our aim isn't to follow the individual gyration of the particle in motion, but rather to describe its path over extended trajectories. For this purpose, the particle behavior is separated between the circular motion about the "guiding center" and the motion of the "guiding center" itself, as shown in Fig. 1.5a. The guiding center is the center of the helical path followed by the particle, which varies continuously over time.

Using these coordinates, and expanding $\vec{B}(\vec{r})$ in a Taylor series about \vec{R} to the first order, we obtain the equations:

$$\dot{\vec{R}}_{\perp} = \hat{e}_1 \times \left(\frac{mv_{\perp}^2}{2qB^2} \nabla B + \frac{m}{Bq} v_{\parallel}^2 \frac{\partial \hat{e}_1}{\partial s} \right) \quad (1.8)$$

$$\frac{d\vec{v}_{\parallel}}{dt} = -\frac{1}{2} \frac{v_{\perp}^2}{B} (\nabla B)_{\parallel} \quad (1.9)$$

, where in Eq. 1.8, \hat{e}_1 is the direction of the magnetic field \vec{B} (as shown in Fig. 1.5a), and s is the distance measured along the field line. The two different terms of the equation are called respectively *gradient drift* and *curvature drift*. The gradient drift term is perpendicular to \vec{B} and $\nabla \vec{B}$, so it carries particles along lines of constant \vec{B} ; the curvature drift term results in a drift velocity $\vec{v}_c \propto \hat{n} \times \vec{B}$, perpendicular to the magnetic field and to its line of curvature (Fig. 1.5b). Eq. 1.9 shows that the guiding center of the particle is accelerated in the opposite direction of the gradient of the magnetic field, so a particle moving into a stronger field will eventually be repelled, regardless of its charge or the direction of the magnetic field. This effect is called *mirroring* (or *bouncing*) and a region of high magnetic field is called *magnetic*

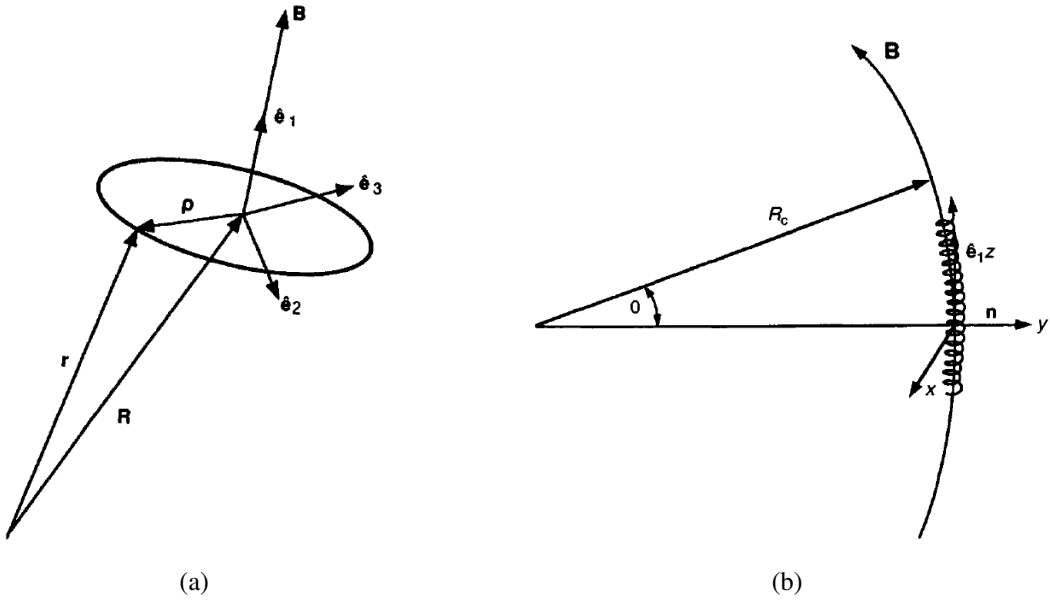


Figure 1.5: (a) Visualization of the guiding center coordinates, where ρ describes the motion about the guiding center and R describes the motion of the guiding center itself. [24], Fig. 2.3.

(b) Visualization of the curvature drift, where a charged particle following a curved magnetic field \vec{B} (with curvature radius R_c) gets drifted in the \hat{x} direction. [24], Fig. 2.5.

mirror (or mirror points).

The three motions of trapped particles

The three magnetic effects of *gradient drift*, *curvature drift* and *mirroring* are the primary controlling factors leading to long-term trapping. The scale size of the magnetosphere is large compared to the gyroradii of the trapped particles, so the magnetic field they experience during gyration is almost uniform. Thus, an energetic particle introduced into the geomagnetic field circles about the field direction while moving parallel to the field line. The parallel motion will take the particle towards the poles of the Earth, where the increased magnetic field intensity causes the particle to be reflected. This bounce motion is superimposed on the much slower curvature and gradient drifts, perpendicular to the magnetic field and to its gradient in the plane perpendicular to the field. If the Earth's field were symmetric about the polar axis, these drifts would be entirely in the longitudinal direction. However, distortion in the geomagnetic field alters this result, and the drifts will have components in the latitude and altitude directions. For the Earth, the gradient and curvature drifts are eastward for electrons and westward for protons. This motion is visible in Fig. 1.6, where the size of the gyroradius is exaggerated for clarity. [23], [24], Chap. 2.

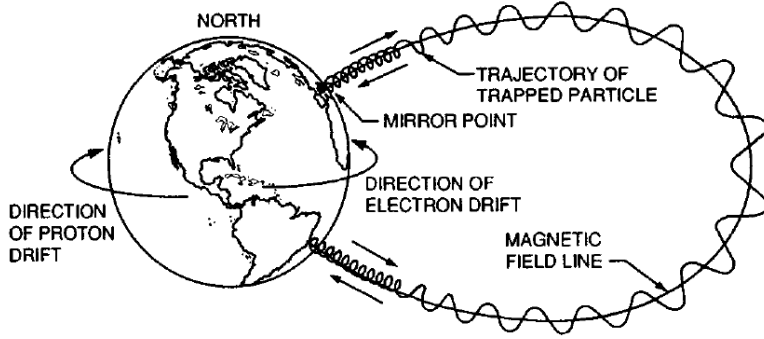


Figure 1.6: Visualization of the trajectory of a trapped particle in the geomagnetic field, showing the bounce motion of the guiding center and the circular motion of the particle around the field line. The curvature drift is indicated by the arrows. [24], Fig. 2.7.

The Adiabatic Invariants

These three motions correspond to three *adiabatic invariants*, quantities "almost conserved" that allow long-range prediction of particle location. These quantities are constant, provided the forces directing the motion are altered adiabatically. The three adiabatic invariants are defined starting from the classical action variable, the integral of the canonical momentum p over a complete cycle:

$$J = \oint_C p(x) dx \quad (1.10)$$

By using the canonical momentum for a particle in a magnetic field, $\vec{P} = \vec{p} + q\vec{A}$, where \vec{A} is the vector potential, we can obtain the three different adiabatic invariants, integrating through three different paths.

By integrating around the gyration orbit, we obtain $J_1 = \pi p_{\perp}^2 / qB$; the first invariant is the magnetic moment: $\mu = p_{\perp}^2 / 2mB$, which corresponds to J_1 , except for constant factors. Using the pitch angle α , we can derive $p^2 \sin^2(\alpha) / B = \text{constant}$; in the absence of an electric field, p^2 is constant, and so we see that as a particle moves towards earth, the field increases, and so does the pitch angle, until it reaches 90° and the particle reflects its trajectory, at a maximum magnetic field value B_m .

The second periodic motion is the bounce between mirror points, if the longitudinal drift is small during a single bounce, the action variable associated with the bounce motion will be constant. By integrating over a bounce the action integral, we obtain the second invariant, called J :

$$J = \oint_C (\vec{p} + q\vec{A}) \cdot d\vec{s} = \oint_C \vec{p} \cdot d\vec{s} = \oint_C p \cos(\alpha) ds = \oint_C p_{\parallel} ds \quad (1.11)$$

, where the integral of $q\vec{A}$ is zero because the integration path along the field line encloses a negligible area, and no magnetic flux, so

$$\oint_C q\vec{A} \cdot d\vec{s} = q \int \nabla \times \vec{A} \cdot d\vec{\Sigma} = q \int \vec{B} \cdot d\vec{\Sigma} = 0 \quad (1.12)$$

, where $\vec{\Sigma}$ is the area enclosed by the bounce path, and α is the drift angle, the angle between the magnetic field lines and the particle momentum.

The invariance of J ensures that a particle will return to the original field line after bouncing. The last periodic motion is the longitudinal drift about the Earth; in a static field, the first two conserved quantities will ensure that the particle returns to its original field line and will specify the field line occupied by the particle at each latitude, but p may change with trajectory and magnetic field. The last constant of motion is needed to define trajectories in slowly changing magnetic fields; as before, it is obtained by integrating the action , this time over the longitudinal drift path, at the equator. The result is $J_3 = q\Phi$, where Φ is the flux of the magnetic field over the drift path. Since the flux needs to remain constant, slow compressions or expansions of the magnetic field will cause trapped particles to move inward or outward [24], Chap. 4.

Particles in the radiation belts

The description of trapped radiation around Earth involves large populations of particles distributed in space with different energies and pitch angles. The physical quantity used to characterize this system is the particle flux, which is closely related to the output of most radiation detectors. The differential directional flux at location \vec{r} , for a given energy and direction, is defined as the number of particles with energy in the interval $[E, E + dE]$ crossing a unit area (dA), perpendicular to the given direction (defined by the angle θ), within a unit solid angle ($d\Omega$) per unit time (1s):

$$dN(\vec{r}, E, \theta) = j(\vec{r}, E, \theta) dA dE d\Omega \quad (1.13)$$

where $dN(\vec{r}, E, \theta)$ is the rate of particle passing through a unit area, with given energy, direction, and location, and $j(\vec{r}, E, \theta)$ is the differential directional flux. For particles trapped in the magnetosphere, the most convenient reference direction is the geomagnetic field vector, so flux is often expressed in terms of the pitch angle α .

Other definitions of flux, used in astrophysics since they are more closely related to the measurements of the detectors, are:

- The omnidirectional flux: $j(E) = \int_{\Omega} j(E, \alpha) d\Omega = \int_0^{\pi} j(E, \alpha) 2\pi \sin(\alpha) d\alpha$
- The integral flux: $j(\alpha, E > E_0) = \int_0^{\infty} j(\alpha, E) dE$
- The integral, omnidirectional flux: $j(E > E_0) = \int_{E_0}^{\infty} dE \int_0^{\pi} j(\alpha, E) 2\pi \sin(\alpha) d\alpha$

The radiation belts can be characterized by the particle species, their energy spectra, and their spatial distributions. When we need to estimate these properties, computational models of the fields are used; the most accurate are NASA's AE9 and AP9 models, which are described in Sec. 1.4. These models do not provide exact particles distributions at any given time, because of the system's dynamical nature, but still capture the overall distributions of trapped particles around Earth.

Protons are concentrated in magnetospheric regions where the geomagnetic field supports trapping. In Fig. 1.7 the contours of omnidirectional integral proton fluxes above 100 keV and 50 MeV are shown. In both cases, the intensity contours become more closely spaced below $L = 1.5R_e$, where Earth's atmosphere is dense enough to remove energetic protons. Moreover, increasing the energy threshold shifts the flux maximum closer to Earth. At these altitudes, asymmetries in the geomagnetic field distort the contours of radiation intensity. Since trapped particles follow lines of constant \vec{B} , differences between hemispheres lead to significant flux variations at low altitudes.

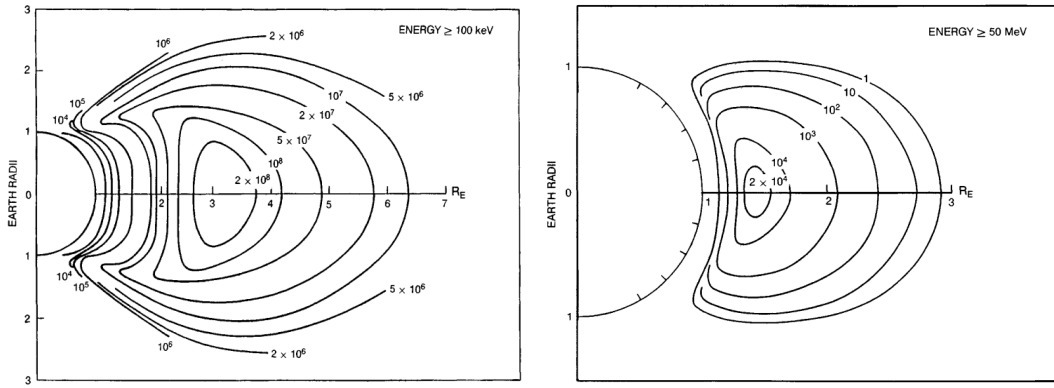


Figure 1.7: On the left: contours of omnidirectional integral proton fluxes above 100 keV. [24], Fig. 5.10. On the right: contours of omnidirectional integral proton fluxes above 50 MeV. [24], Fig. 5.12.

The different contour lines represent different values of the omnidirectional integral particle flux, indicated in the figure in units of particles/ $(s \cdot cm^2)$.

The region of the Southern hemisphere between South America and Africa has a weaker surface magnetic field, and is known as the *South Atlantic Anomaly*. Here, particles descend to lower altitudes, resulting in much higher radiation intensities than in other areas at the same latitude.

Electrons are another major population of trapped particles, with energies extending up to several MeVs. Their average flux strongly depends on geomagnetic activity; for this reason, different models are employed for different phases of the solar cycle. Fig. 1.8 shows equatorial values of integral omnidirectional electron fluxes for varying energy thresholds. It is evident that flux decreases rapidly with increasing energy. The slot at $L \simeq 2.5R_e$, more pronounced at higher energies, is likely caused by enhanced electron loss rates in this region. Finally, heavier ions are also present in the radiation belts, typically remaining near the equatorial plane. Oxygen and helium ions, in the range between 1 and 50 keV, are particularly abundant, especially during magnetically active periods. [24], Chap. 5.

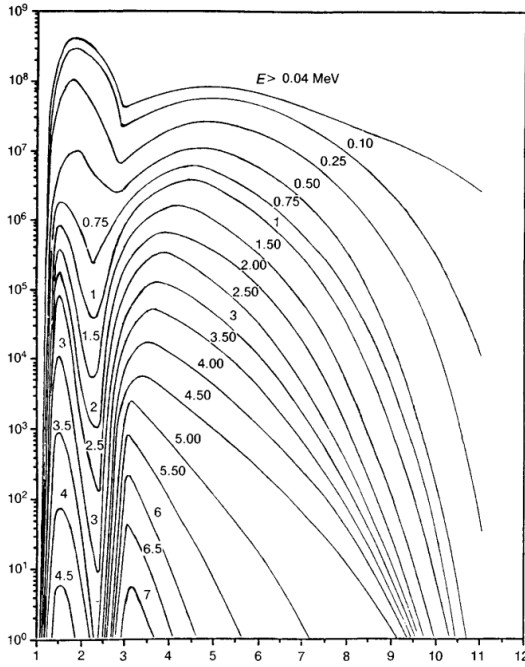


Figure 1.8: Equatorial values of the integral, omnidirectional electron flux above various energy thresholds (E), in units of particles/ $(s \cdot cm^2)$. The radius of sampling (x-axis) is in units of R_e . [24], Fig. 5.15.

1.2 The CSES mission

The China Seismo-Electromagnetic Satellite (CSES) is a collaborative scientific mission between China and Italy designed to study the near-Earth space environment. Its primary goal is to monitor electromagnetic fields, plasma, and particle perturbations in the topside ionosphere, with particular attention to possible correlations with seismic activity.

In addition to this main objective, the mission also addresses a broader range of scientific themes. These include the investigation of the structure and dynamics of the topside ionosphere, as well as the study of coupling mechanisms between the lower and higher plasma layers, which are essential for understanding energy transfer processes in geospace. The mission further contributes to the monitoring of temporal variations in the geomagnetic field, both during quiet periods and under disturbed conditions caused by solar activity.

Another important aspect of the CSES mission is the observation of fluctuations and temporal variations in the fluxes of trapped particles, analyzed in relation to the evolution of space weather. Finally, the satellite plays a key role in exploring solar-terrestrial interactions and transient phenomena, such as Coronal Mass Ejections (CMEs), solar flares, and the solar modulation of cosmic rays.

The CSES constellation, now comprehensive of two different satellites, CSES-01 and CSES-02, will be able to provide continuous, multi-point, accurate monitoring of the Earth's ionosphere. Indeed, it will advance our understanding of the LAIC (Lithosphere–Atmosphere

–Ionosphere Coupling) both for phenomena originating in the Earth’s Atmosphere and Lithosphere, possibly related to seismic activity, and for those originating in the Earth’s magnetosphere directly related to Sun Activity.

The first satellite launched was CSES-01, launched on February 2nd, 2018, which follows a Sun-synchronous orbit with 97,4° inclination at an altitude of 507 km. Despite its small dimensions, 750 kg distributed in a volume of 2.75 m³, it contains a lot of important payloads, reported in Table 1.1. Figure 1.9a shows a visualization of the satellite.

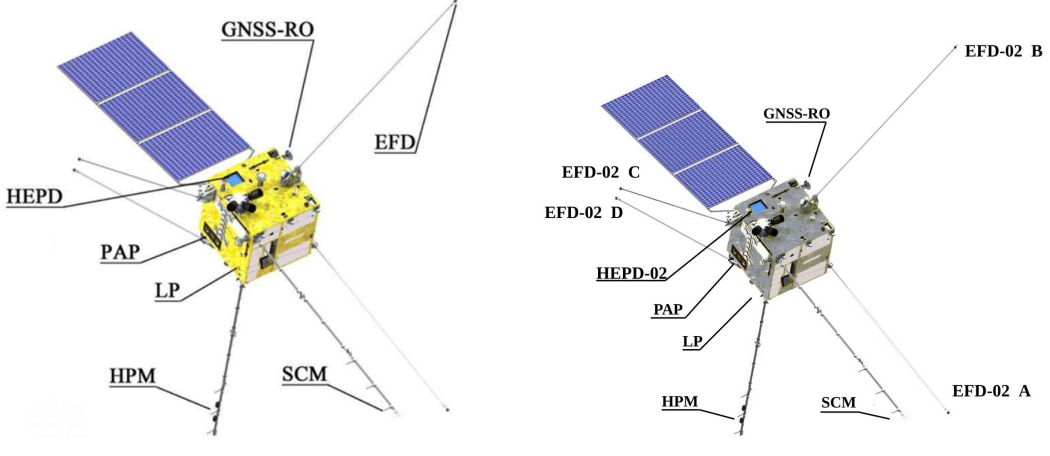
Category	Payload Name	Observation Target
Energy Particle	High Energy Particle Detector (HEPD-01)	Proton: 30 MeV ~ 200 MeV Electron: 3 ~ 100 MeV
	High Energy Particle Package (HEPP)	Electron: 25 keV ~ 3.2 MeV
Electro-Magnetic Field	Electric Field Detectors (EFD)	Electric Field: DC ~ 3.5 MHz
	High Precision Magnetometer (HPM)	Magnetic Field: 10 Hz ~ 20 kHz
	• Vector Magnetic Field: FGM1, FGM2	
	• Scalar Magnetic Field: CDSM, CPT	
In Situ Plasma	Search Coil Magnetometer (SCM)	Magnetic Field: 10 Hz ~ 20 kHz
	Plasma Analyzer Package (PAP)	Composition: H ⁺ , He ⁺ , O ⁺ Ni: 5 × 10 ² ~ 1 × 10 ⁷ cm ⁻³ Ti: 500 K ~ 10000 K
	Langmuir Probe (LP)	Ni: 5 × 10 ² ~ 1 × 10 ⁷ cm ⁻³ Ti: 500 K ~ 10000 K
	GNSS Occultation Receiver	TEC by transmit VH/U/L Signal
Plasma Profile Construction	Tri-Band Beacon	TEC by transmit VH/U/L Signal
	Ionospheric	O ₂ 135.6 nm and N ₂ LBH airglow

Table 1.1: CSES-01 payloads, with their main characteristics and their observation targets. [14].

The CSES-02 mission (Fig. 1.9b) was launched on June 14th, 2025, with similar objectives to its predecessor. It is built on the same CAST2000 satellite platform as CSES-01, with several enhancements. It follows the same orbital plane of CSES-01 with a 180° phase shift, enabling a complementary ground track. This configuration effectively reduces the revisit time from 5 days to 2.5 days, significantly improving temporal resolution and correlation capabilities, and establishing a new dual-satellite system for ionospheric monitoring. Unlike CSES-01, whose payload operations were initially limited to latitudes between ±65° (later expanded to ±70°), CSES-02 has enabled full-orbit payload operation, greatly enhancing coverage and broadening the range of scientific investigations. The CSES-02 carries nearly the same suite of scientific payloads as CSES-01, each featuring specific technological upgrades, along with two additional instruments to enhance observational capabilities.

In particular, for measurements of particle energy, it has two new modules, HEPD-02 and MEED (Medium Energy Electron Detector), an upgrade of the HEPD-01 and the HEPP.

For magnetic field measurements, it has an SCM (Search-Coil Magnetometer), an HPM (High Precision Magnetometer), and an EFD-02 (Electric Field Detector). For in situ plasma detection, it has PAP (Plasma Analyzer Package) and Languimir Probes. For plasma profile construction, it has a GNSS Occultation Receiver and a Tri-Band Beacon. Finally, for ionospheric measurements, it has an Ionospheric Photometer.



(a) Visualization of the CSES-01 Satellite. [14]. (b) Visualization of the CSES-02 Satellite. [15].

The High-Energy Particle Detector (HEPD-01), part of the CSES-01 satellite mission, operated in the highest energy range among the onboard instruments, detecting electrons (3–100 MeV), protons and light nuclei (30–300 MeV/n) up to Oxygen. Throughout its continuous operation, HEPD-01 provided valuable data on various natural phenomena.

It measured the cosmic-ray proton spectrum between 40 and 250 MeV and monitored its temporal evolution until June 2022. The detector captured detailed information on the October 28, 2021, Ground Level Enhancement, including proton spectra and arrival times. HEPD-01 also observed changes in low-energy particle populations during geomagnetic storms in August 2018 and May 2021.

The instrument contributed to the study of the Earth's inner radiation belt, estimating trapped proton populations as functions of energy, pitch angle, and L-shell³, consistent with the NASA AP9 model. It analyzed the trajectories of re-entrant albedo protons (<250 MeV) in Low-Earth Orbit, confirming the stability of these populations and validating past results from PAMELA and AMS-01. Additionally, HEPD-01 monitored the South Atlantic Anomaly, revealing a geographic shift in its center between 2018 and 2022.

Astrophysical observations included the detection of Gamma-Ray Bursts, identified through secondary low-energy electron excesses. [6], [13], [14], [17], [19].

³The L-shell is a parameter describing a set of planetary magnetic field lines; intuitively, it can be viewed as the set of magnetic field lines that cross the Earth's magnetic equator at a distance, in Earth radii, equal to the L-value. [12].

1.3 The new pixel tracker of the High Energy Particle Detector (HEPD-02) on board the CSES-02 satellite

HEPD-02 is designed to detect individual particles, identify their type (proton, electron, nucleus), measure their energy, and determine their pitch angle. Its main objective is to detect particle bursts, sudden flows of particles falling from the inner Van Allen belt, and to accurately determine their energy spectrum and magnetospheric origin, aiming to explore potential temporal correlations with seismic events on Earth. HEPD-02 is composed of five subsystems: Detector (DES), Mechanics (MES), Electronics (ELS), Power Supply (PSS), and Harness (HAS). Its key general and technical requirements are summarized in Table 1.2.

Parameter	Value
Operating temperature range	$-10^{\circ}\text{C} \div +35^{\circ}\text{C}$
Operating pressure	$\leq 6.65 \times 10^{-3} \text{ Pa}$
Data budget	$\leq 100 \text{ Gb/day}$
Mass budget	$\leq 50 \text{ kg}$
Power budget	$\leq 45 \text{ W}$
Electron kinetic energy range	$3 \text{ MeV} \div 100 \text{ MeV}$
Proton kinetic energy range	$30 \text{ MeV} \div 200 \text{ MeV}$
Angular resolution	$\leq 10^{\circ}$ for e^- with $E > 3 \text{ MeV}$
Energy resolution	$\leq 10\%$ for e^- with $E > 5 \text{ MeV}$
Pointing	Zenith
Scientific data bus	RS-422
Data handling bus	CAN 2.0
Life cycle	$> 6 \text{ years}$

Table 1.2: General and technical requirements of the HEPD-02 instrument. [5].

The Detector is formed by different components, shown in Fig. 1.10. The Direction Detector (DD, Tracker) measures the entrance angle of incoming particles using ALPIDE MAPS, originally developed at CERN. It includes five independent turrets, each with three stacked sensor planes (staves) composed of 10 ALPIDE chips. The sensors are bonded to carbon-fiber cold plates and read out via flexible circuits. Each turret connects to a tracker splitter board for data interface. The Trigger Detector (TD) consists of two segmented plastic scintillator planes (TR1 and TR2) read out by Hamamatsu PMTs. TR1 is placed before the DD and segmented into 5 bars along the Y-axis; TR2 is placed after the DD and segmented into 4 bars along the X-axis. The structure minimizes material to reduce pre-measurement interactions and uses CFRP supports to reduce weight. The Energy Detector (ED) consists of a calorimeter combining 12 plastic scintillator planes (RAN, Range Calorimeter) and 2 layers of LYSO crystal scintillators (EN, Lyso Calorimeter) for range and energy measurement, respectively. RAN layers are $150 \times 150 \times 10 \text{ mm}^3$ and read out by 2 PMTs each; EN layers are segmented LYSO bars ($150 \times 49 \times 25 \text{ mm}^3$), oriented orthogonally between planes and

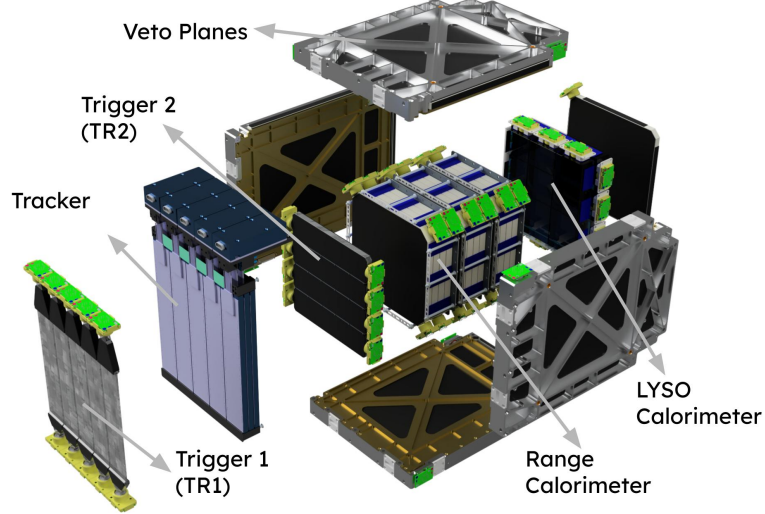


Figure 1.10: Exploded view of the HEPD-02, with its different components visualized. [16].

also read out by PMTs. Finally, the Containment Detector (CD, Veto Planes) is composed of 5 plastic scintillator panels: 4 lateral (LAT) and 1 bottom (BOT), each 8 mm thick and read out by two PMTs. It tags events with particles entering or escaping from the sides or bottom, helping to identify and discard incomplete or contaminating measurements.

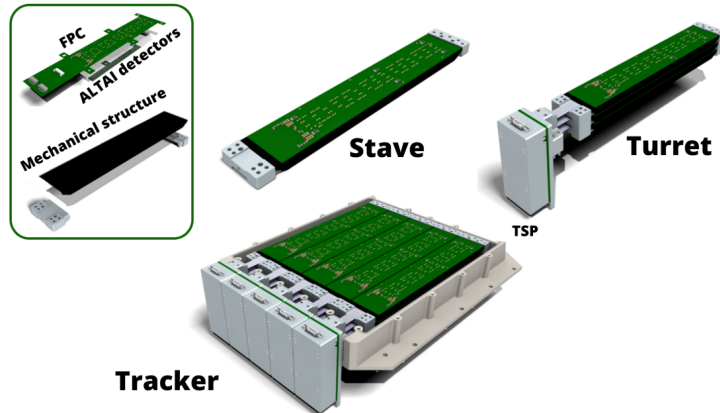


Figure 1.11: Visualization of the structure of the tracker inside HEPD-02. [18].

In particular, the HEPD-02 Direction Detector is the first experiment to use Monolithic Active Pixel Sensors (MAPS) in its pixel detector, for tracking particles in space. MAPS is a technology at the forefront of research in the field, where the detector and readout electronics are integrated on the same silicon wafer. To effectively implement this technology, it was necessary to design the tracker system from scratch, paying particular attention to power consumption, temperature control, mechanical stability, and material budget minimization.

The tracker utilizes ALTAI chips, which serve as a building block; they are an updated version of ALPIDE chips, featuring a pixel pitch of $28\mu\text{m}$ and a resolution of 0.5 Mpx each. The structure of the detector is shown in Fig. 1.11. The sensors are glued and wire-bonded onto a Flexible Printed Circuit (FPC), which distributes power and clock signals and gathers the readout. A pile of three staves, separated by 8.5mm , forms a turret, and the detector is formed by 5 turrets placed side by side, at a distance of 4.5mm . The total active area of the sensor is $15 \times 15\text{ cm}^2$. [5], [20].

1.4 State-of-the-art in trapped particle flux modelling

The *AE9* (for energetic electrons) and *AP9* (for energetic protons), together with the Space Plasma Model (SPM), represent the current state-of-the-art in trapped radiation environment specification. Developed by the Air Force Research Laboratory (AFRL) under the IRENE project (International Radiation Environment Near Earth), these models are based on an extended database of more than 30 satellite missions (over 300 satellite-years of data), covering different solar cycle phases. This is a major improvement compared to the historical AE8/AP8 models, which relied on data from only about 20 satellites collected between the 1960s and 1970s. The main advantages of AE9/AP9 are:

- Extended coverage in both energy and spatial domains, with electrons up to tens of MeV and protons up to several GeV.
- Statistical robustness through Monte Carlo simulations, which provide median, 50%, and 95% confidence levels. This enables realistic “worst-case” environment estimates for mission design.
- Improved resolution in geographic and magnetic coordinates, giving more accurate maps of particle fluxes and fluences.
- Continuous updates, with several versions released since 2012, incorporating new missions (e.g. Van Allen Probes, Azur), new functionalities (dose calculation kernels, epoch dependence), and performance improvements.

The models provide particle flux maps for both electrons and protons. Figs. 1.12 and 1.13 show representative examples of the AE9 electron flux distribution and the AP9 proton flux distribution, at different Energy thresholds (E), with a confidence level (CL) of 50%.

A key aspect is that AE9/AP9 are continuously validated with new satellite data and under new solar conditions. For instance, comparisons between AP9 predictions and in-orbit measurements from the HEPD instrument onboard CSES-01 in the South Atlantic Anomaly show generally good agreement, though some discrepancies remain at the boundaries of the anomaly. Fig. 1.14 shows an example of the measurements that are possible with HEPD-01, in particular, it shows the trapped particle distribution, used to map the SAA.

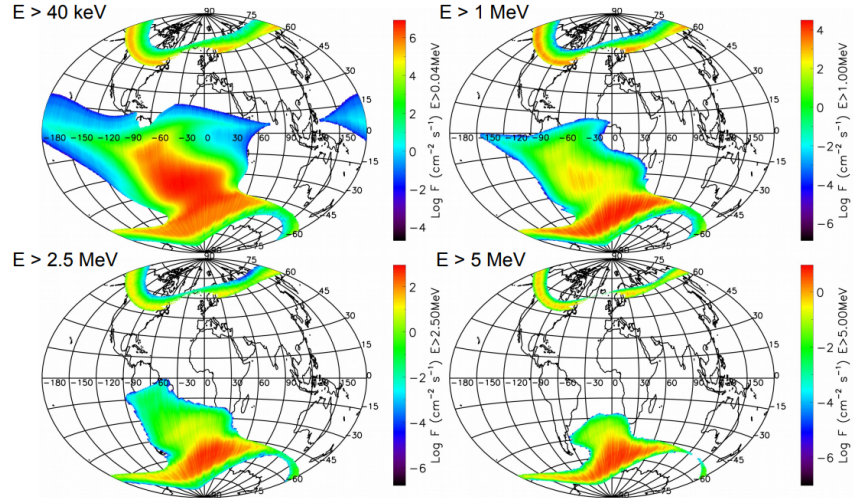


Figure 1.12: Electron integral flux maps from AE9, at different energy thresholds (E), 50% CL. [19]

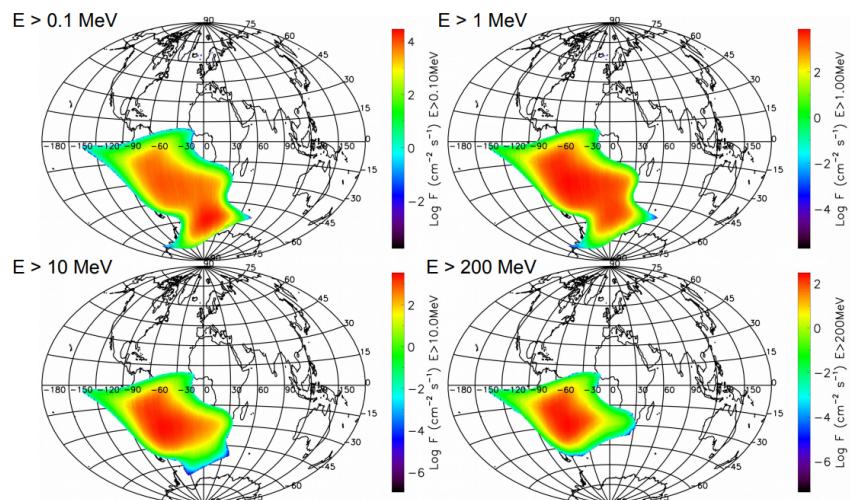


Figure 1.13: Proton integral flux maps from AP9, at different energy thresholds (E), 50% CL. [19].

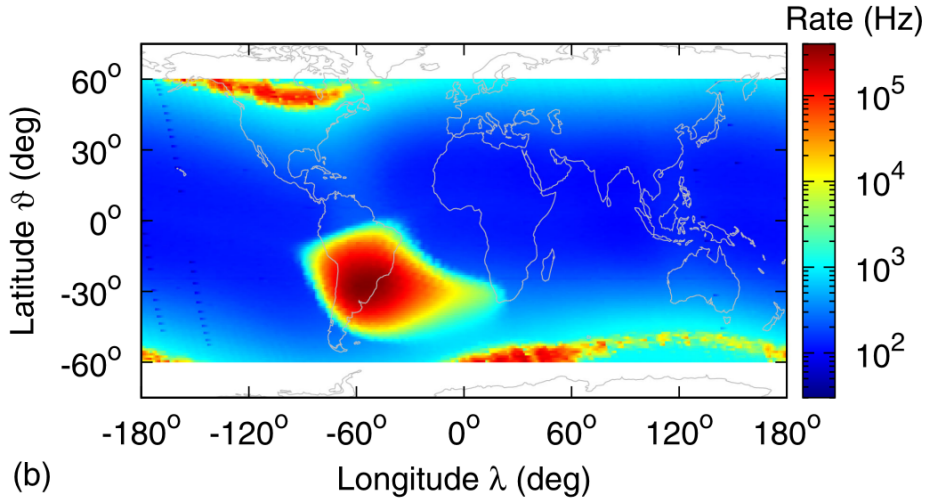


Figure 1.14: Mapping of the SAA, from the rate of particles detected by HEPD-01. [6].

To maintain model reliability for current and future space missions in the evolving solar conditions, the ongoing validation and updates are of key importance. In this context, HEPD-02 and its particle tracker are essential: during a single trigger event, multiple particles can enter the detector, in high-occupancy conditions; therefore, a sensor without a tracker may provide energy measurements that are not representative of the actual particle population. On the other hand, HEPD-02, thanks to track reconstruction, can determine the number of particles being detected, allowing the data used to update the models to be more accurate, even in these high-occupancy conditions. [6], [19].

Chapter 2

Track reconstruction methods

2.1 Tracking technologies and track reconstruction methods

Tracking is an important technique in particle physics, since it can be used in different physical analyses: it allows one to determine the particle trajectory, it can help identify the hitting particle by estimating the energy loss (dE/dx)¹ passing through the active area of the sensor, and it can be used to estimate a charged particle's impulse by measuring its curvature under a magnetic field. In the case of the HEPD-02, it can help determine the region of origin of the particles moving in the Van Allen belts, thus giving deeper insights into the dynamics of the trapped particles.

Modern physics experiments use a variety of detection techniques, each optimized for a specific purpose. Table 2.1 shows the spatial resolution, time resolution, and dead time² for some of these detectors, which will be described in more detail later. [25], 35.1 .

Multi-Wire Proportional and Drift Chambers

Multi-Wire Proportional Chambers (MWPCs) and drift chambers are modern gaseous detectors based on the principle of single-wire proportional counters. MWPCs, introduced in the late 1960s, consist of a grid of parallel anode wires placed between cathode planes, allowing detection, localization, and energy measurement of charged particles over large

¹The mean rate of energy loss by charged heavy particles passing through matter is described by Bethe's equation:

$$-\langle \frac{dE}{dx} \rangle = K z^2 \frac{Z}{A} \frac{1}{\beta^2} \left[\frac{1}{2} \ln \left(\frac{2m_e c^2 \beta^2 \gamma^2 W_{\max}}{I^2} \right) - \beta^2 - \frac{\delta(\beta\gamma)}{2} \right]$$

where K a constant with units of $[cm^2/mol]$, z is the charge number of the incident particle, Z is the atomic number of the absorber, A is the atomic mass of the absorber (g/mol), $\beta = v/c$ is the velocity of the particle relative to the speed of light, $\gamma = 1/\sqrt{1-\beta^2}$ is the Lorentz factor, $m_e c^2$ is the electron rest energy, W_{\max} is the maximum kinetic energy transferable in a single collision, I is the mean excitation energy of the absorber material, and $\delta(\beta\gamma)$ is the density effect correction, important at high energies. [10], 34.2.3 .

²Dead time: the time a detector requires to register an event.

Detector Type	Spatial Resolution (rms)	Time Resolution	Dead Time
Resistive plate chamber	50 μm	50–1000 ps	10 ns
Liquid argon TPC	0.5–1 mm	0.01–1 μs	–
Scintillation tracker	\sim 100 μm	100 ps	10 ns
Bubble chamber	10–150 μm	1 ms	50 ms
Wire chambers (proportional and drift)	50–100 μm	5–10 ns	20–200 ns
Micro-pattern gas detector	30–40 μm	5–10 ns	20–200 ns
Silicon strips/pixels	\lesssim 10 μm	few ns	\sim 50 ns

Table 2.1: Different Detectors, classified by their typical Spatial Resolution, Time Resolution and Dead Time. [25], 35.1 .

areas. Electrons produced by ionization drift toward the wires and generate avalanches, which are read out to determine the particle positions. Typical position resolution reaches tens of micrometers for tracks perpendicular to the wire plane.

Drift chambers, developed in the early 1970s, exploit the drift time of electrons to reconstruct the coordinate perpendicular to the wire plane. Field-shaping wires improve charge collection and linearity, enabling precise spatial measurements. Advanced implementations, such as Time Projection Chambers (TPCs), extend these concepts to three-dimensional tracking and particle identification. These detectors are fundamental in high-energy physics experiments, offering large-area coverage with precise tracking capabilities. [25], 35.6.2 . One of the experiments using MWPCs was the DELPHI experiment, located at the Large Electron Positron Collider (LEP), at CERN. [9]. Drift chambers, on the other hand, are used in various experiments, including the ATLAS experiment at the Large Hadron Collider (LHC) at CERN. [4].

Micro-Pattern Gaseous Detectors

Micro-Pattern Gaseous Detectors (MPGDs) emerged in the late 20th century as a response to the intrinsic limitations of wire-based detectors, such as diffusion effects and space-charge buildup, which constrained their spatial resolution to 50–100 μm . Advances in microelectronics and photolithography enabled the development of novel gas detectors with high rate capability (up to 10^6 Hz/mm²), spatial resolutions down to 30 μm , nanosecond timing, radiation hardness, and cost-effectiveness for large-area coverage.

However, long-term operational instabilities, such as charging-up, aging, and micro-discharges, limited its practical application and motivated the development of more robust structures such as the Gas Electron Multiplier (GEM) and the Micromegas.

A GEM is a thin metal–insulator–metal foil perforated with microscopic holes, where charge multiplication occurs. By cascading multiple GEM foils, high gains ($> 10^4$) can be achieved

while reducing discharge risks. Micromegas detectors instead use a micromesh above a narrow amplification gap, providing excellent spatial resolution ($\approx 12 \mu\text{m}$) and fast signals thanks to efficient ion evacuation. Both technologies surpass traditional MWPCs in rate capability by orders of magnitude.[25] 35.6.4 . The CMS at CERN is one of the experiments using GEMs, to track muons. [8].

Time Projection Chambers

The Time Projection Chamber (TPC), invented in the 1970s, is based on a cylindrical or square field cage filled with a gaseous or liquid detection medium. Charged particles produce ionization electrons that drift in a uniform electric field towards an amplification stage, providing a 2D projection of the track. The third coordinate is derived from the drift time of the electrons, measured relative to an external trigger. Gas-filled TPCs are widely used in accelerator-based experiments due to their low material budget, while liquid TPCs are favored for neutrino and rare event searches requiring large active masses.

The TPC enables full 3D reconstruction of charged particle trajectories, offering superior pattern recognition compared to detectors with only 2D planes. This is particularly advantageous in environments with high track multiplicities, such as heavy-ion collisions. Particle identification is possible by combining momentum measurements, obtained from helical fits in a magnetic field, with the specific energy loss (dE/dx). The latter is estimated from multiple charge samples along the track.[25], 35.6.5. The ALICE experiment, at CERN, uses gaseous TPCs to track and identify particles. [2].

Resistive Plate Chambers

Resistive Plate Chambers (RPCs) are gaseous detectors operating at atmospheric pressure, developed in the early 1980s as an alternative to large-area scintillation counters. They are based on two high-resistivity planar electrodes, separated by spacers defining a gas gap. A uniform electric field of several kV/mm induces avalanche multiplication of the primary electrons produced by the interaction of ionizing radiation with the gas.

RPCs can operate in two modes: *avalanche*, which features good rate capability and proportional signals, and *streamer*, which produces nearly constant amplitude signals but with limited rate capability. The signal induced by avalanches is collected by external metallic electrodes, often structured as strips or pads. The position can be reconstructed with the charge barycenter method. With centimeter-scale strip pitches, the spatial resolution is essentially geometric, while with analog charge readout, it can reach a few tens of microns. Their performance are listed in the table 2.1 . However, their rate capability is limited by the voltage drop across the resistive electrodes, which depends on resistivity, thickness, and average avalanche charge.

In summary, RPCs combine high efficiency, good space-time resolution, and the ability to

cover large areas, adapting to a variety of applications in high-energy physics, from muon detection to time-of-flight measurements, as well as to new developments in calorimetric detectors and searches for new physics. [25], 35.6.7 . RPCs are used, for example, in the CMS experiment at CERN. [8].

Silicon-Based Sensors

Semiconductor detectors provide excellent spatial, energy, and time resolution, often simultaneously. In accelerator experiments, they are primarily used as position-sensing devices in tracking detectors or as photodetectors in calorimeters and imaging Cherenkov detectors. Pixel sensors operate in the following way: a particle hitting the active area of the sensor transfers some of its energy to the electrons of the Si atoms in the detector. Since silicon is a semiconductor with a band-gap of $\simeq 3.6\text{eV}$, some of the electrons in the material are excited into the conduction band, forming electron-hole pairs that can move under a potential difference. A MIP³ typically creates 89-106 couples per μm of active material crossed. The free charge created is collected by the sensor in $\simeq 10\text{ns}$ for scales of $\simeq 100\mu\text{m}$, thanks to the elevated electron mobility, and the signal is analyzed by the reading electronics. If it overcomes the threshold value, the hit is saved. There are lots of possible noise factors with these types of sensors: typically, the charge produced by a single hit is spread across different pixels, and the hit gets smeared. By doing clustering on the activated pixels, the resolution on the hit position can overcome pixel pitch. Thermal excitation can cause the release of electrons in the conduction band, without any hit, and imperfections in the material can have a similar effect; the fake hits problem can be partially solved by tuning the threshold value or excluding hits that activate single pixels in the clustering procedure, but it may cause the rejection of real hits. [25], 35.8.1 . HEPD-02 is the first detector using a MAPS silicon tracker in a space mission. [5].

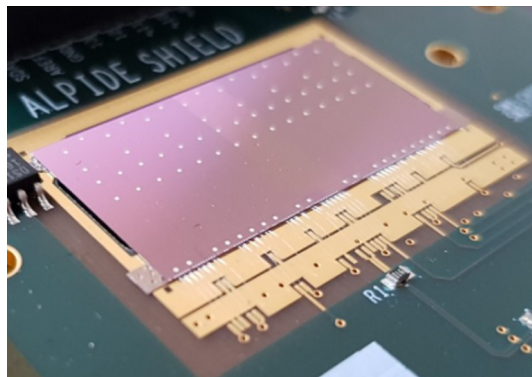


Figure 2.1: Visualization of a silicon-based MAPS ALPIDE chip. [3].

³Minimum Ionizing Particle, embodies the minimum ionizing loss in substances.

Scintillating Fiber Trackers

Scintillating Fiber Trackers (SciFi) use thin scintillating fibers to detect energetic particles, with signals read out via multi-channel photo-detectors such as Silicon Photo-Multipliers (SiPMs). The scintillating fibers produce and transport light when traversed by charged particles, resulting in tens of photons emitted per hit.

Some challenges of the scintillating fibers include the scintillating dye, which must be radiation-hard, and the light attenuation length, which must be limited to prevent signal loss. Fiber shapes can be cylindrical or rectangular and are positioned in the plane of the detector surface, perpendicular to the direction of incoming particles. A charged particle passing through the detector generates photons in multiple fibers, which in turn produce avalanches in the pixels. These signals are used to reconstruct the particle track, achieving spatial resolutions down to $\sim 10 \mu\text{m}$, as in the CHORUS experiment, a vertex tracker for detecting τ leptons, which used $20 \mu\text{m}$ capillary fibers filled with liquid scintillator. [7], [25], 35.1. The KEK To Kamioka (K2K) experiment has used SciFi as a neutrino tracker, and SciFi trackers were also used in ATLAS to complete its detector. [4], [11].

2.2 Tracking Reconstruction Algorithms

After obtaining the signal from a particle hit, the problems related to tracking are not yet solved. The signals, containing both hit and noise information, need to be interpreted by algorithms in order to detect the original particle track. We will focus on tracking algorithms applied to a three-layer silicon detector, as in the case of HEPD-02. In particular, the track reconstruction algorithms analyzed in this thesis are:

- Combinatorial Method: easiest to implement, but more susceptible to missed hits and high occupancy of the detector.
- Hough Transform Method: needs more computational resources, scalable to high occupancy with high miss probability.

2.2.1 Combinatorial Method

This method aims to reconstruct the best-fitting line through the detected hit points, based on the lowest χ^2 evaluation.

For a detector with n layers, the dataset is divided into all possible combinations of n points, one from each layer. A linear fit is performed for every group of hits, and the χ^2 is calculated for each fit, using the formula:

$$\chi^2 = \sum_{i=1}^n \frac{\|\vec{y}_i - \vec{f}(\vec{x}_i)\|_2^2}{\sigma^2} \quad (2.1)$$

where $\vec{f}(\vec{x}_i)$ are the values of the best-fitting line, evaluated at the points $\{\vec{x}_i\}_{i=1}^n$ of the group. The line is given by: $\vec{f}(\vec{x}) = M\vec{x} + \vec{q}$, where \vec{x} is the position inside the detector, M is the coefficient matrix that represents the line direction, and \vec{q} is the offset of the line at $\vec{x} = 0$. Finally, σ denotes the uncertainty associated with the points in the dataset, which can correspond to the resolution error of the detector employed.

The HEPD-02 tracker is composed of three active layers vertically stacked along the z-axis, with a spacing of 8.5 mm between each layer. For reconstruction purposes, each layer can be considered infinitely thin, so hit points lie in a (x-y) plane, with three possible z-values. For this reason, the equations above can be adapted for this specific case:

- The fit function, parametrized on the z-value, can be written as:

$$\begin{pmatrix} x(z) \\ y(z) \\ z(z) \end{pmatrix} = \begin{pmatrix} v_x \\ v_y \\ v_z \end{pmatrix} (z - z_0) + \begin{pmatrix} x_0 \\ y_0 \\ z_0 \end{pmatrix} \quad (2.2)$$

where the first term after the equal sign is the direction of the line \vec{v} , and the last term is a point on the line, obtained from the dataset.

- the points $\{\vec{x}_i\}_{i=1}^3$ where the fit function can be evaluated are $\{z_i\}_{i=1}^3$ corresponding to the values 0mm, 8.5mm, 17mm.
- The χ^2 (Eq.2.1) can be calculated with:

$$\chi^2 = \sum_{i=1}^n \frac{\left\| \begin{pmatrix} x_i \\ y_i \\ z_i \end{pmatrix} - \begin{pmatrix} x(z_i) \\ y(z_i) \\ z(z_i) \end{pmatrix} \right\|_2^2}{\sigma_{x-y}^2} = \sum_{i=1}^n \frac{\left\| \begin{pmatrix} x_i \\ y_i \\ z_i \end{pmatrix} - \left[\vec{v}(z_i - z_0) + \begin{pmatrix} x_0 \\ y_0 \\ z_0 \end{pmatrix} \right] \right\|_2^2}{\sigma_{x-y}^2} \quad (2.3)$$

The parameter σ_{x-y} is the uncertainty on the location of each hit in a layer of the detector. It corresponds to the resolution error of the ALTAI chip, given by $\sigma_{x-y} = 28 \mu\text{m}/\sqrt{12}$, where the numerator is the pixel pitch of the sensor.

- The number of points considered in each fit (n) is expected to be two or three, depending on whether the reconstruction involves a missed point. Events containing a singlet are extremely rare and cannot be reconstructed. In Eq. 2.3, since (x_0, y_0, z_0) is a point in the dataset, the expected value for the χ^2 is 2 when $n = 3$. When the considered combination is a doublet, $n = 2$, the χ^2 value is always null.

After evaluating all χ^2 values for the different combinations of points, the line with the smallest χ^2 is selected as the best fit. If this value is below the fixed threshold, the corresponding points are considered successfully reconstructed and are excluded from the dataset. The threshold is set to $\chi^2 = 6$, corresponding to a probability of $P(\chi^2 \leq 6) \simeq 0.95$. The procedure is then repeated on the remaining points until the dataset is empty.

If, at some stage, all possible three-point combinations yield a χ^2 larger than the chosen threshold, the algorithm continues by forming pairs of points. Finally, if only a single point remains, it is classified as not reconstructed, since a track cannot be inferred from a single hit. [1].

Fig. 2.2 is a schematic representation of the combinatorial algorithm's operation, where the dashed lines represent the original tracks of the hitting particles, and the solid lines represent their reconstruction attempted by the algorithm. On the left, the red line illustrates an incorrect combination of points, including points from both the light blue and blue dashed lines. This reconstruction produces a line that deviates significantly from the considered points, causing the χ^2 of the fit to exceed the threshold, and thus the combination is discarded. On the right, the green line shows a correct combination, where the reconstructed line deviates from the points only within the smearing uncertainty. The χ^2 of this combination will be below the threshold, and if no other combinations have a lower value in this iteration, the points will be reconstructed correctly.

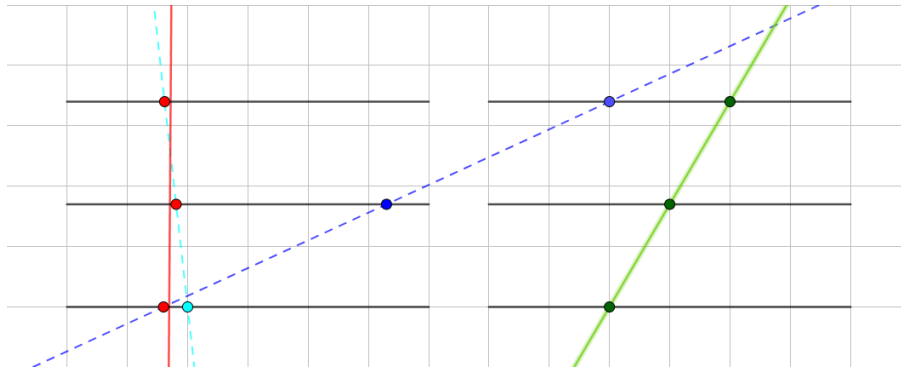


Figure 2.2: Visualization of two reconstruction attempts using the combinatorial method. The dashed lines represent the tracks followed by the hitting particles, while the solid lines represent the reconstruction attempts. The red solid line represents an incorrect reconstruction, while the green solid line represents a correct reconstruction.

2.2.2 Hough Transform Method

The second reconstruction algorithm implemented was the Hough Transform, a standard method for detecting structures within a cluster of points based on their parametric equations. In the context of track recognition, the Hough Transform attempts to reconstruct lines from points by mapping them from the point space into the line-parameter space. For a 3D detector, this is done separately on each projection plane, working in 2D, and the best fit among the three projections is then selected for the final reconstruction.

In particular, after projecting all the hit points on a given plane ($x-y$, $x-z$ or $y-z$), the Hough transform uses polar coordinates, describing each point (x, y) as $(\rho \cdot \cos(\theta), \rho \cdot \sin(\theta))$, where $\rho = \sqrt{x^2 + y^2}$ and $\tan(\theta) = y/x$. The relation $\rho = x \cdot \cos(\theta) + y \cdot \sin(\theta)$ holds for each different hit point, and from this, a unique $\rho(\theta)$ curve can be derived. Fixed (x_0, y_0) , different

points of the same $\rho(\theta)$ curve correspond in the (x, y) plane to different lines passing through the same point; each line can be described with (ρ, θ) , where these parameters are, in order, the minimum distance between the origin and the line and the angle between the origin and ρ , as reported in Fig. 2.3.

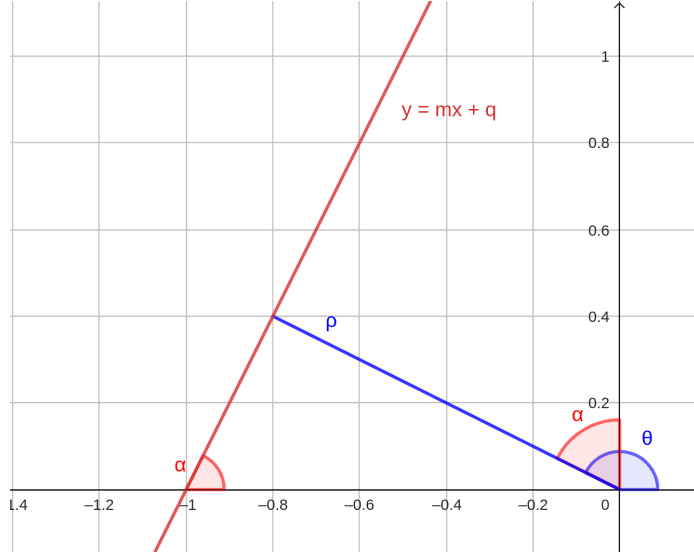


Figure 2.3: Visualization of the (ρ, θ) parameters, in the case of a line with a positive slope value, $m > 0$, $\tan(\alpha) > 0$.

When we plot the $\rho(\theta)$ curve of two or more different (x_i, y_i) points from the same line, these curves intersect at $(\bar{\rho}, \bar{\theta})$, which can be used to determine their generating line, with the equation:

$$y(x) = -\frac{1}{\tan(\bar{\theta})}x + \frac{\bar{\rho}}{\sin(\bar{\theta})} \quad (2.4)$$

As reported in the Fig. 2.3, it is important to note that $\bar{\theta}$ isn't the angle between the line and the x-axis (α in the figure), so this equation should be motivated mathematically. We shall remember the equation of a line passing through two points (x_0, y_0) , (x_1, y_1) :

$$y(x) = \frac{y_1 - y_0}{x_1 - x_0}(x - x_0) + y_0 \quad (2.5)$$

which can also be expressed in the form $y(x) = mx + q$ where $m = \frac{y_1 - y_0}{x_1 - x_0}$ is slope of the line, $\tan(\alpha)$, and $q = \frac{x_1 y_0 - x_0 y_1}{x_1 - x_0}$ is the vertical offset at $x = 0$.

Considering the intersection of two $\rho(\theta)$ curves, and using $(\rho_0, \theta_0) = (\rho_1, \theta_1) = (\bar{\rho}, \bar{\theta})$, we can write:

$$\begin{aligned} x_1 \cdot \cos(\bar{\theta}) + y_1 \cdot \sin(\bar{\theta}) &= x_0 \cdot \cos(\bar{\theta}) + y_0 \cdot \sin(\bar{\theta}) \\ \implies \tan(\bar{\theta}) &= \frac{x_1 - x_0}{y_0 - y_1} = -\frac{1}{\tan(\alpha)} \end{aligned}$$

Using this result in Eq. 2.4, we get the correct slope of the line, m . For the coefficient q , we can evaluate $\bar{\rho}/\sin(\bar{\theta})$, obtaining the correct expression reported in Eq. 2.5.

In the case of $\tan(\alpha) < 0$, the same steps can be repeated, leading to the correct result.

The Hough transform method uses this mathematical property to determine which points are in the same line; after using the polar coordinates transformation on the projected hit points, the (ρ, θ) plane is divided in discrete bins, and the plots of $\rho(\theta)$ are produced for every point (x_i, y_i) . The number of curves passing in each bin is then counted, and the bin with the highest count is selected to reconstruct the line. The line is reconstructed via linear regression, with a maximum of three points for each line, the number of planes of the detector. This reconstruction is repeated in each projection plane, and the best-fitting line of all three planes is chosen for the next step; if its χ^2 is below the acceptance threshold, the points are excluded, and the process is repeated until the number of points is 2 or less.

2.3 Prospects in Tracking with Deep Learning Methods

Graph Neural Networks (GNNs) are a central method within the broader field of geometric deep learning, representing trainable functions that operate on graphs: sets of elements and their pairwise relations. GNNs are highly expressive and have demonstrated superior performance compared to traditional deep learning approaches in various domains. Data in particle physics is often intrinsically heterogeneous and sparse in space, which means it does not naturally conform to homogeneous or grid-like data structures typically required in others deep learning techniques; instead, they can be naturally expressed as unordered sets of elements with rich relations and interactions, making graphs a suitable representation. This approach offers key advantages for particle physics by overcoming the limitations of representations like images or sequences, which might impose non-intrinsic orderings on the data, thereby reducing learning performance.

GNNs address the particle tracking problem by formulating it as an edge classification task:

- **Graph Construction:** Each sparse measurement or hit is represented as a node in the graph. Edges are constructed between pairs of hits that exhibit geometrically plausible relations.
- **Learning Process:** The GNN model employs multiple updates of node representations and edge weights across the graph. During the training, the edge weights are updated, indicating the relative importance of different connections.
- **Task Output:** The GNN learns to identify which edges truly connect hits belonging to the same particle track.

This GNN approach has demonstrated high accuracy in simplified cases and shows promise for more realistic scenarios. GNN models that utilize message passing have been used to improve performance in track reconstruction. [21].

Chapter 3

Dataset and results

3.1 Pseudo-dataset generation

When this work was initiated, CSES-02 had not yet been launched, so it was necessary to create a dataset resembling the one that HEPD-02 would produce using computational simulations. This dataset was required to test the different track reconstruction algorithms, and thus, a dataset of hitting particles was generated through a toy Monte Carlo simulation. The first task was to reproduce the detector, with its real geometry; the active area of the detector was reproduced in a python environment, recreating five turrets divided in three layers, each with 10 ALTAI chips. Real gaps between different turrets (l_{Lgap}) and between chips (l_{sgap}) were used to reconstruct the active area. Afterward, random lines were generated with two different angular distributions, representing particles hitting the detector with varying incident angles. Only the lines that would result in "good hits" were saved. Specifically, those corresponding to particles that reached the bottom of the detector without leaving the active area through the sides. The intersections between these lines and the active area were recorded as hits. If a track passed through the small gaps between pixels or the larger gaps between different turrets, the hit would be considered missing, but to avoid an excessive number of doublets or singlets, such tracks were regenerated. In the simulation, the stave was set to be two dimensional, and all the hits obtained in the same plane would have the same height ($z = 0, 8.5, 17$ mm). In the real detector, it is unlikely that only a single pixel is activated after being hit by a particle; instead, the hit is smeared across several different pixels. To recreate this effect, after the hit generation, a Gaussian error was added in the two dimensions x and y, the plane of the stave, with a distribution defined by μ and σ_{x-y} . Furthermore, it isn't always the case that an incoming particle is detected by the device; for this reason, a varying miss probability was added to the simulation. Finally, thermal noise perturbations can cause fake pixel activation, and to simulate this effect, randomly generated noise points were added to the dataset, with a probability of P_{noise} . The dataset was saved in a .csv file, where the first column was used as an event index, going from 1 to N_{gen} ; the columns 2, 3 and 4 were used to save the hit mark x, y and z coordinates, and finally the fifth

column was used to save the index of the line generating the points, this index was a number going from 1 to the number of simultaneous hits, N_{hits} . Table 3.1 reports the values of the parameters used in the simulation.

Parameter	Value
A_{stave}	30mm \times 150mm
z_{dist}	8.5mm
l_{Lgap}	4.85 mm
l_{sgap}	0.15 mm
N_{gen}	1000
N_{hits}	[1 : 10]
μ	0 mm
σ_{x-y}	$28\mu\text{m}/\sqrt{12} \simeq 8\mu\text{m}$
P_{miss}	$[0.05, 10^{-6}]$
P_{noise}	10^{-6}

Table 3.1: Parameters used in the toy Monte Carlo simulation.

Two different particle direction distributions were used: an isotropic distribution and an inclined distribution. These two are described by their angular profiles, reported in Figs. 3.2 and 3.3, that are derived from two datasets of 10 thousand lines. The convention used for spherical coordinates is the one represented in Fig. 3.1.

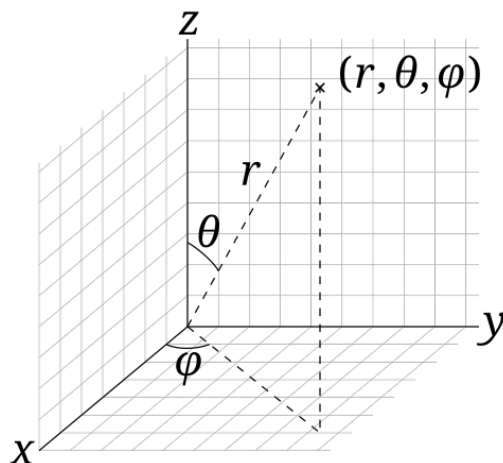


Figure 3.1: Visualization of the 3D spherical coordinates convention used. Where r is the distance from the origin, θ is the polar angle, and ϕ is the azimuthal angle. [22].

Angular components are derived from Cartesian coordinates using the following formulas:

$$\theta = \arccos(z/r)$$

$$\varphi = \arctan(y/z)$$

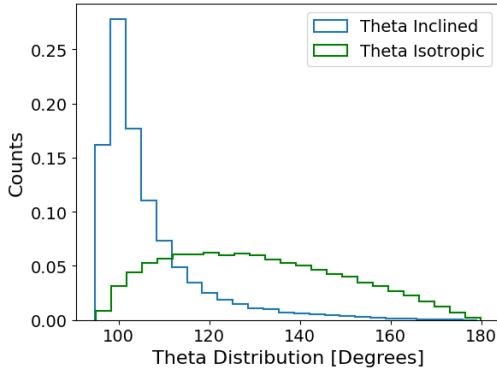


Figure 3.2: Visualization of the theta angle distribution in the generated directions datasets.

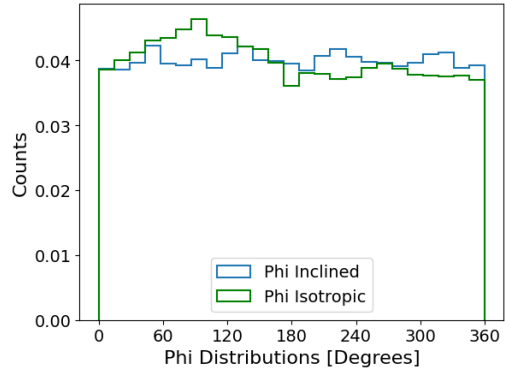


Figure 3.3: Visualization of the phi angle distribution in the generated directions datasets.

The distribution of the phi angle is quasi-homogeneous in both generations, with the deviations coming from the geometry of the detector. In fact, the detector isn't homogeneous in phi, since it is a rectangle (15×17 cm) with gaps between turrets where the hit isn't registered. On the other hand, theta varies in the two different generations: in the inclined one, values of theta near 90° are more present, while in the isotropic distribution, the values are more uniformly distributed.

Different types of dataset were created: starting with one track per event up to ten simultaneous tracks per event. For each dataset, one thousand events were simulated. The hits generated were saved using an index to indicate the event of origin, and another one to indicate which of the generated lines they were part of. In this way, after applying the path reconstruction algorithms, it was possible to check if the groups of points obtained were correct or not; and so the track reconstruction efficiency of each algorithm was evaluated, with respect to the number of simultaneous hits in the detector.

3.2 Results on simulated data

The dataset was used to test the combinatorial and Hough transform reconstruction algorithms.

Combinatorial Method:

The combinatorial method has proven to be highly robust when all hit points of each track are present in the dataset. If all three hit points of a given track are available, the algorithm will eventually evaluate the correct combination, which will precisely represent the original line. Since the method considers all possible combinations of hits across layers, a group of hits generated by the same track will always be included among the evaluated candidates. In such cases, the corresponding χ^2 value depends solely on the smearing coefficient, as all hits

are generated by the same line. This results in a significantly lower χ^2 compared to other combinations, allowing the algorithm to correctly identify the track using the "minimum χ^2 " criterion.

However, the situation changes when only two hit points are detected for a given track. Because any two points define a line, combinations involving two hits yield χ^2 values below the threshold, regardless of whether the hits originate from the same particle. As a result, the reconstruction becomes non-deterministic and depends on the order in which point pairs are evaluated.

This effect is illustrated in Fig. 3.4, in comparison with Fig. 3.5. These figures show the average efficiency of the reconstruction algorithm on inclined and isotropic datasets, with the number of simultaneous hits ranging from 1 to 10, and with two different values of P_{miss} . The efficiency is computed as:

$$\text{Eff} = \frac{n_{cor}}{n_{tot}} \quad (3.1)$$

where n_{cor} is the number of tracks correctly reconstructed in a single event, where all points in the selected combination are produced from the same hitting particle, and n_{tot} is the total number of tracks per event.

In Fig. 3.4, the hit miss probability was set to $P_{miss} = 0.05$. Since each track is generated with three hits, this corresponds to a 15% chance of producing only a doublet of hits. Consequently, some tracks were reconstructed based on two points, leading to an increase in incorrect associations.

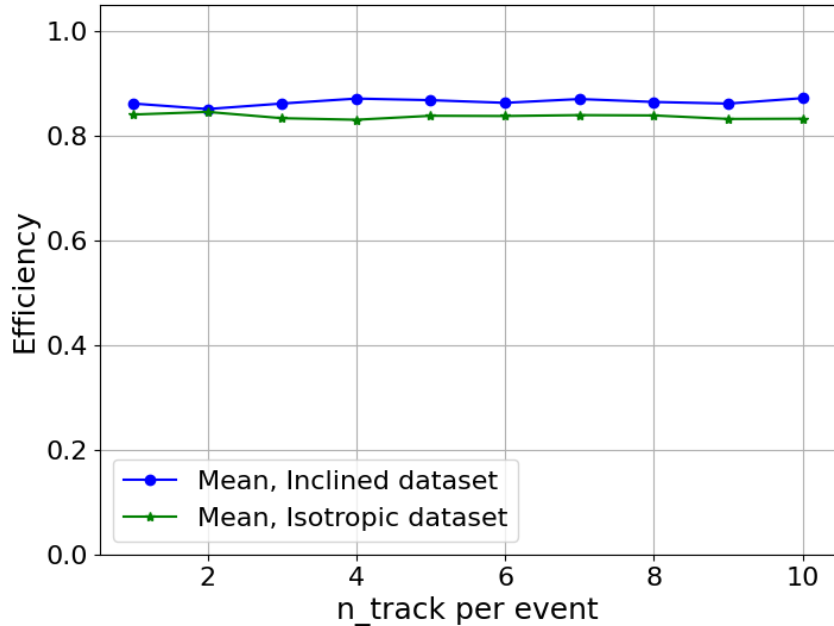


Figure 3.4: Reconstruction efficiency of the combinatorial method, with a miss probability of $P_{miss} = 0.05$.

In contrast, in Fig. 3.5, the miss probability was set to $P_{miss} = 10^{-6}$, resulting in tracks that almost always include all three hits. This improves the reconstruction performance, as the correct combination is more frequently identified, leading to higher efficiency. Furthermore, the algorithm's efficiency never reaches 1, even in events with only one track. This is likely due to a threshold on χ^2 that is too conservative.

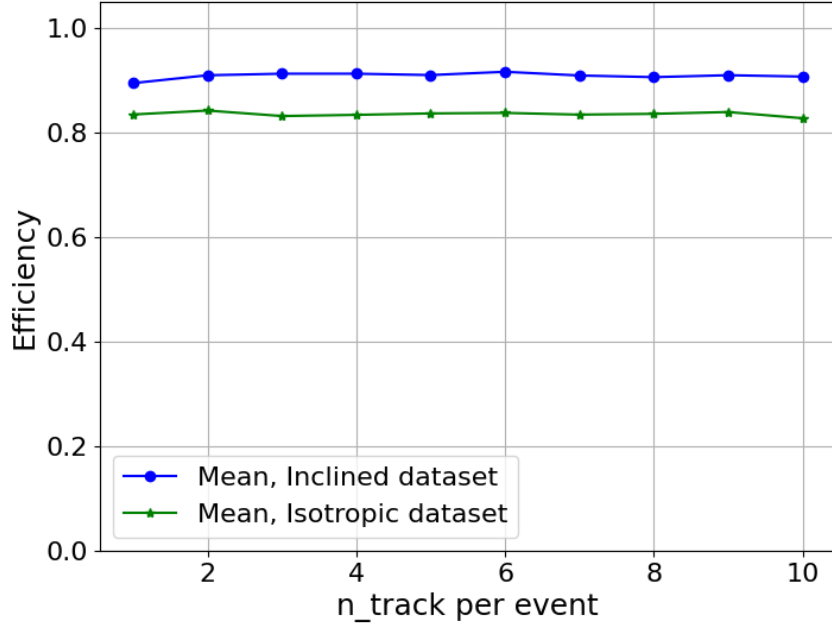


Figure 3.5: Reconstruction efficiency of the combinatorial method, with a miss probability of $P_{miss} = 10^{-6}$.

The number of possible combinations scales with a power of N , the number of distinct tracks in the event. Assuming no missing hits¹, there are N possible points to choose from per layer, yielding a total of $N \times N \times N = N^3$ combinations. As a result, the algorithm's computational cost grows cubically with the number of tracks, as shown in Fig. 3.8. Consequently, this method is not well-suited for the high-occupancy environments.

Hough Transform Method:

The Hough Transform reconstruction algorithm demonstrates greater robustness in scenarios with missing hits, due to its distinct operational principles. The results shown in Figs. 3.6 and 3.7 exhibit a similar trend across the two different P_{miss} values.

The isotropic dataset has a significant impact in the case of higher P_{miss} , where the algorithm is still able to achieve efficiencies comparable to those observed in the low P_{miss} scenario. However, the efficiency of the algorithm decreases as the number of simultaneous hits increases. This is because the larger number of curves in the parameter space can result

¹The fraction of missing hits is below 0.1% of N and thus negligible in this estimate.

in intersections between hits generated by different particles, potentially leading to false reconstructions.

In this method, increasing the number of tracks per event does not substantially affect the computation time per iteration, as shown in Fig. 3.8. Therefore, the algorithm remains suitable for high-occupancy environments without compromising its performance.

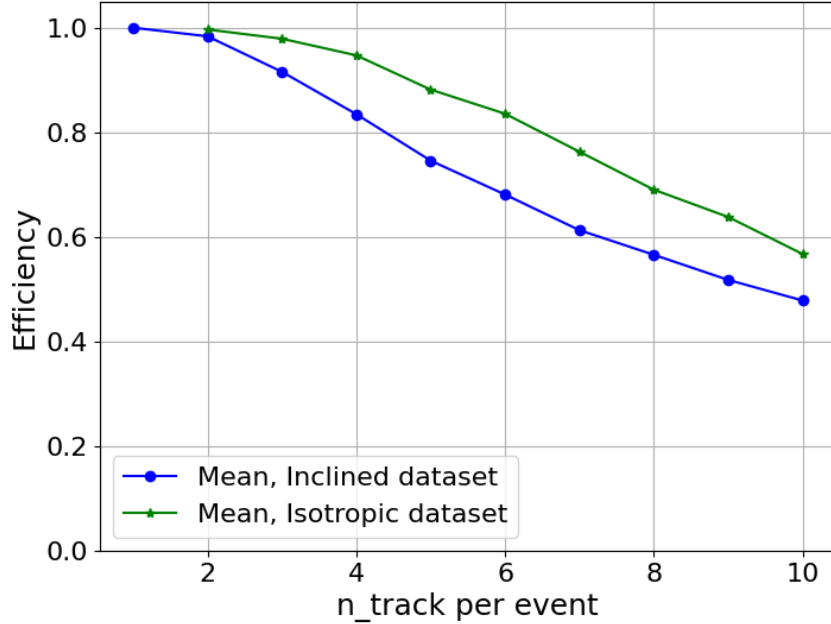


Figure 3.6: Reconstruction efficiency of the HT method, with a miss probability of $P = 0.05$.

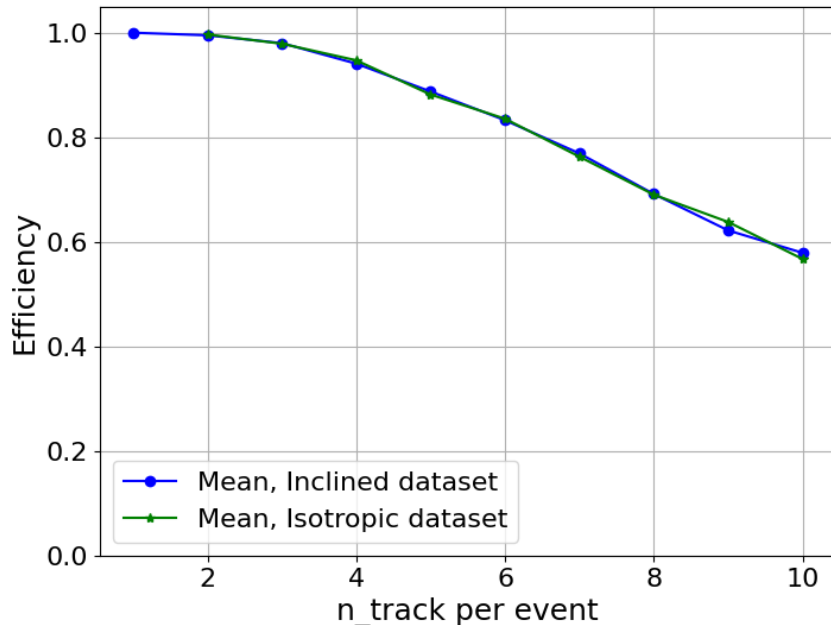


Figure 3.7: Reconstruction efficiency of the HT method, with a miss probability of $P = 10^{-6}$.

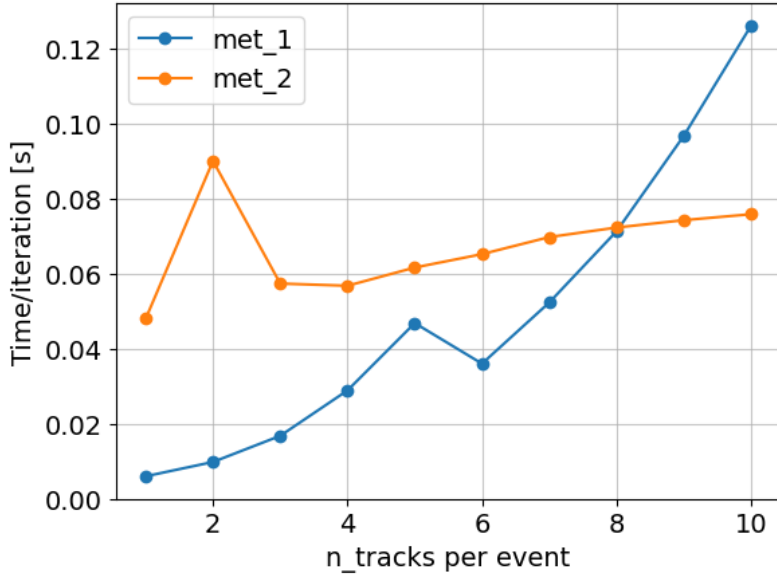


Figure 3.8: Time consumption per iteration of the combinatorial method (`met_1`) and HT method (`met_2`). The y-axis reports the total time spent for the reconstruction of the dataset, over the number of tracks analyzed. $y(n) = t(n)/(n * 1000)$, since each dataset contained 1000 events.

Track reconstruction visualization:

The following figures represent four different events with 10 simultaneous tracks, and the reconstructed lines obtained with the algorithms.

In Fig. 3.9 (a), the brown line represents a false reconstruction, and the pink points are not correctly reconstructed. In Fig. 3.9 (b), the gray and light green lines, constructed with two points, are incorrect, as is the singlet light blue point. This illustrates that the combinatorial method is not suitable for reconstructing point doublets in situations with high miss probabilities. In the first case, it reconstructed a three-point line instead of multiple two-point lines, which would have been correct. In the second case, the lines formed by pairs of points were also incorrect. In contrast, Figs. 3.10 (a) and 3.10 (b) highlight the limitations of the HT method in high-occupancy environments. The use of only one plane for track reconstruction is problematic in such environments because tracks that appear to represent the projection of points in a plane are not always accurate representations of the points in 3D space. This is evident in the red line in Fig. 3.10 (a), which, in the x-y view, appears to be a good reconstruction, but in the other projection does not follow the distribution of the points. On the other hand, this method can reconstruct pairs of points with higher efficiency than the combinatorial approach, as shown by the blue and red lines in Fig. 3.10 (b).

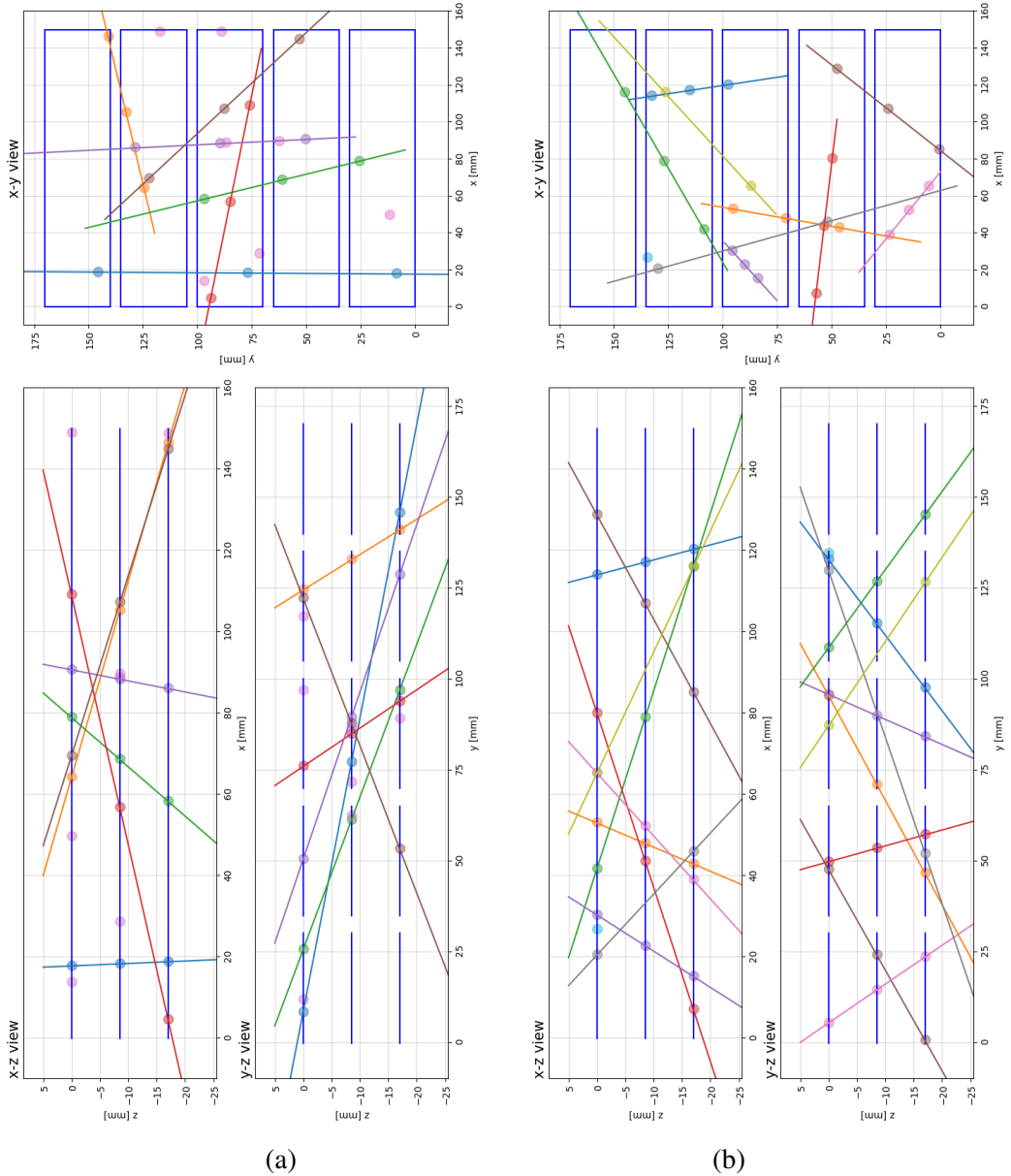


Figure 3.9: Visualization of two events with the combinatorial reconstruction method.

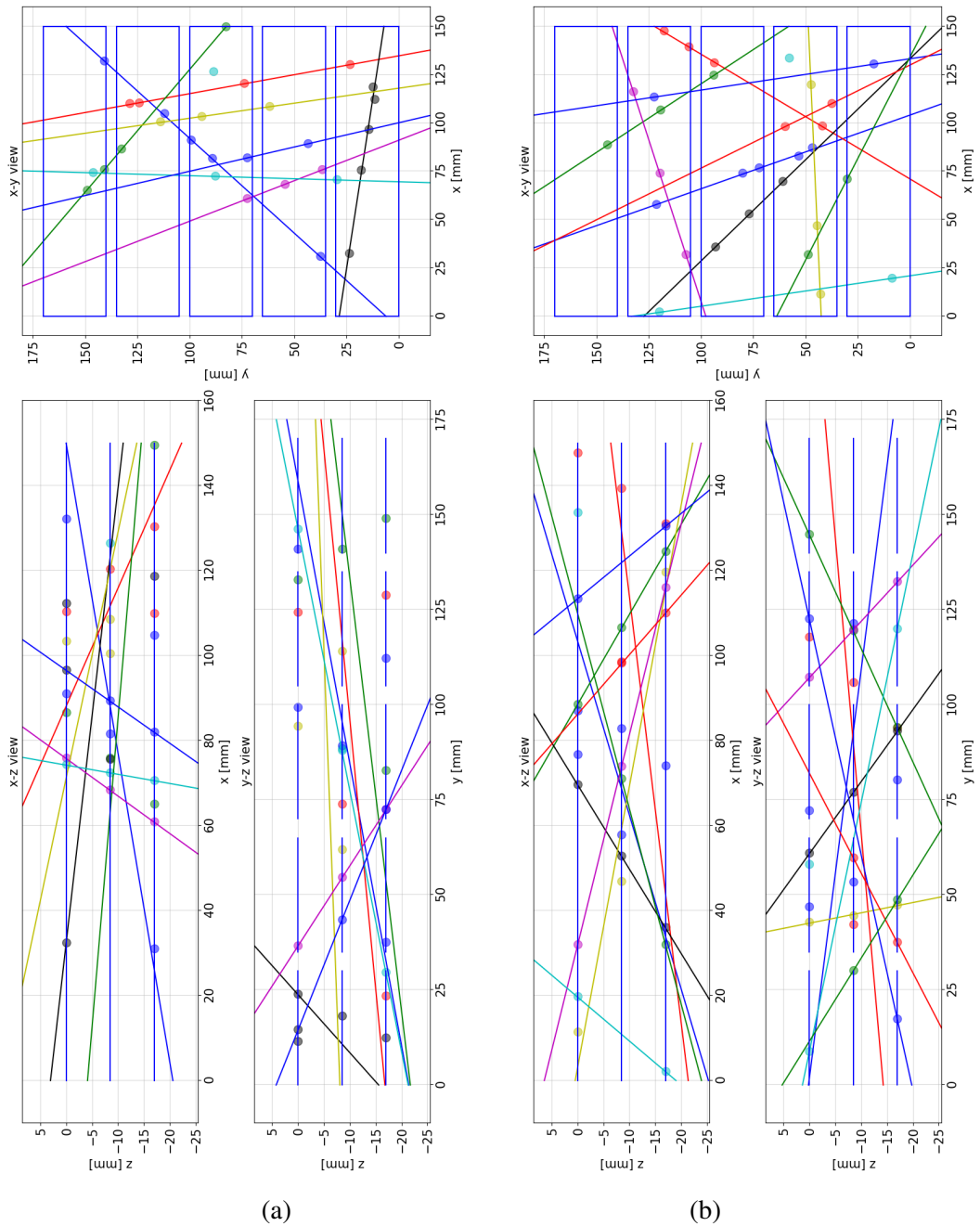


Figure 3.10: Visualization of two events with the Hough Transform reconstruction method.

Conclusions

Tracking in dense environments is a challenging task for both ground-based and space-borne experiments. Such conditions may be encountered by small devices orbiting through the Van Allen Belts or the South Atlantic Anomaly (SAA), as well as by larger detectors, whose active areas can be struck by multiple particles even in relatively low-density regions. Various techniques are employed to record the passage of particles through instrumented materials. We reviewed the most important types of detectors used in modern particle physics experiments to track particles across a wide range of energies and for different purposes. Among them, pixel detectors are a relatively new technology that is enhancing our ability to reconstruct the direction of incoming particles and improve identification performance. In the context of trapped particle flux measurements, the CSES mission is expected to provide valuable results for low-energy protons and electrons. Particles are detected by the High Energy Particle Detectors, which are capable of measuring particle identity, kinetic energy, and arrival direction.

In particular, HEPD-02 is the first pixel tracker to employ Monolithic Active Pixel Sensors (MAPS) for particle tracking in space. Each chip features a pixel pitch of $28\mu\text{m}$ and a resolution of 0.5Mpx . This detector enables high-precision hit position detection, allowing for fine-grained track reconstruction using a variety of reconstruction algorithms.

In this work, we explored and compared two possible methods for reconstructing and distinguishing particles through tracking in high-multiplicity events. The first method, the combinatorial approach, shows stable reconstruction performance as a function of the number of simultaneous tracks (simulated up to 10), with excellent resilience to missing hits caused by pixel inefficiencies. On the other hand, the Hough transform method is faster, especially when the number of points to be fitted grows, but it is less accurate in track reconstruction in events with extremely high multiplicity.

This study can be considered a preliminary comparison between the two methodologies for track reconstruction in scenarios closely resembling the in-flight conditions of HEPD-02. It will serve as a basis for evaluating further developments in the HEPD-02 reconstruction code. Future work should include the integration of deep learning techniques, as discussed in Sec. 2.3, which show promising prospects (e.g., Graph Neural Networks). The next steps will involve using simulated data from the official HEPD-02 Monte Carlo model to improve the fidelity and reliability of the results obtained.

List of Figures

1.1	Visualization of the magnetic fields generated around Earth. The chart shows the different regions described in the main text (i.e., the magnetopause and tails). The action of the solar wind is displayed as well as the presence of the trapped particles and field currents arising in the interaction with the geomagnetic fields. [24], Fig. 1.1.	5
1.2	Visualization of the isointensity lines of the geomagnetic field at Earth's surface. The magnetic field is expressed in units of 10^{-9} T. The chart shows the deviations from the ideal dipole field, with the South Atlantic Anomaly clearly visible and the field lines appearing non-parallel at different latitudes. [24], Fig. 3.2.	6
1.3	Visualization of the Pitch Angle α of a particle in helicoidal motion. α is the angle between the magnetic field \vec{B} , in green, and the particle's linear momentum, in red.	8
1.4	Visualization of the gyration motion of a charged particle. On the left: case with $\vec{B} \neq 0$ and $\vec{E}' = 0$, showing a helical trajectory. On the right: case with $\vec{B}, \vec{E} \neq 0$ and $\vec{B} \perp \vec{E}$, showing an additional drift in the $\vec{E} \times \vec{B}$ direction. [24], Fig. 2.1.	9
1.5	(a) Visualization of the guiding center coordinates, where ρ describes the motion about the guiding center and R describes the motion of the guiding center itself. [24], Fig. 2.3. (b) Visualization of the curvature drift, where a charged particle following a curved magnetic field \vec{B} (with curvature radius R_c) gets drifted in the \hat{x} direction. [24], Fig. 2.5.	10
1.6	Visualization of the trajectory of a trapped particle in the geomagnetic field, showing the bounce motion of the guiding center and the circular motion of the particle around the field line. The curvature drift is indicated by the arrows. [24], Fig. 2.7.	11
1.7	On the left: contours of omnidirectional integral proton fluxes above 100 keV. [24], Fig. 5.10. On the right: contours of omnidirectional integral proton fluxes above 50 MeV. [24], Fig. 5.12. The different contour lines represent different values of the omnidirectional integral particle flux, indicated in the figure in units of particles/($s \cdot cm^2$).	13

1.8	Equatorial values of the integral, omnidirectional electron flux above various energy thresholds (E), in units of particles/($s \cdot cm^2$). The radius of sampling (x-axis) is in units of R_e . [24], Fig. 5.15.	14
1.10	Exploded view of the HEPD-02, with its different components visualized. [16].	18
1.11	Visualization of the structure of the tracker inside HEPD-02. [18].	18
1.12	Electron integral flux maps from AE9, at different energy thresholds (E), 50% CL. [19]	20
1.13	Proton integral flux maps from AP9, at different energy thresholds (E), 50% CL. [19].	20
1.14	Mapping of the SAA, from the rate of particles detected by HEPD-01. [6].	21
2.1	Visualization of a silicon-based MAPS ALPIDE chip. [3].	25
2.2	Visualization of two reconstruction attempts using the combinatorial method. The dashed lines represent the tracks followed by the hitting particles, while the solid lines represent the reconstruction attempts. The red solid line represents an incorrect reconstruction, while the green solid line represents a correct reconstruction.	28
2.3	Visualization of the (ρ, θ) parameters, in the case of a line with a positive slope value, $m > 0$, $\tan(\alpha) > 0$	29
3.1	Visualization of the 3D spherical coordinates convention used. Where r is the distance from the origin, θ is the polar angle, and ϕ is the azimuthal angle. [22].	32
3.2	Visualization of the theta angle distribution in the generated directions datasets.	33
3.3	Visualization of the phi angle distribution in the generated directions datasets.	33
3.4	Reconstruction efficiency of the combinatorial method, with a miss probability of $P_{miss} = 0.05$	34
3.5	Reconstruction efficiency of the combinatorial method, with a miss probability of $P_{miss} = 10^{-6}$	35
3.6	Reconstruction efficiency of the HT method, with a miss probability of $P = 0.05$	36
3.7	Reconstruction efficiency of the HT method, with a miss probability of $P = 10^{-6}$	36
3.8	Time consumption per iteration of the combinatorial method (<code>met_1</code>) and HT method (<code>met_2</code>). The y-axis reports the total time spent for the reconstruction of the dataset, over the number of tracks analyzed. $y(n) = t(n)/(n * 1000)$, since each dataset contained 1000 events.	37
3.9	Visualization of two events with the combinatorial reconstruction method.	38
3.10	Visualization of two events with the Hough Transform reconstruction method.	39

List of Tables

1.1	CSES-01 payloads, with their main characteristics and their observation targets. [14].	15
1.2	General and technical requirements of the HEPD-02 instrument. [5].	17
2.1	Different Detectors, classified by their typical Spatial Resolution, Time Resolution and Dead Time. [25], 35.1	23
3.1	Parameters used in the toy Monte Carlo simulation.	32

Bibliography

- [1] *Algoritmi di Tracciamento per un Rivelatore a Pixel di Silicio a 3 Strati in Ambiente ad Alta Occupanza e Rumore*. URL: <https://docs.google.com/document/d/1-7oDvOKvWP-6tSrumhaniIgSsMJ9Htfo> (visited on 07/21/2025).
- [2] *ALICE*. Aug. 2025. URL: <https://www.home.cern/science/experiments/alice> (visited on 09/07/2025).
- [3] *ALPIDE MAPS sensor*. Aug. 2025. URL: <https://ep-ese.web.cern.ch/project/alice-its> (visited on 09/07/2025).
- [4] *ATLAS*. Aug. 2025. URL: <https://atlas.cern/> (visited on 09/07/2025).
- [5] Luca Barioglio et al. “The Monolithic Active Pixel Sensors Tracker System of the High Energy Particle Detector aboard the Second Chinese Seismo-Electromagnetic Satellite”. In: *IEEE Aerospace and Electronic Systems Magazine* (2025), pp. 1–16. DOI: 10.1109/MAES.2025.3568361.
- [6] S. Bartocci et al. “Mapping the South Atlantic Anomaly charged particle environment with the HEPD-01 detector on board the CSES-01 satellite”. In: *Physical Review D* 111.022001 (2025). DOI: 10.1103/PhysRevD.111.022001. (Visited on 06/25/2025).
- [7] Fred Blanc. *Scintillating Fiber Trackers:recent developments and applications*. <https://cds.cern.ch/record/1603129/files/LHCb-TALK-2013-310.pdf>. Accessed: 25-08-2025.
- [8] *CMS*. Aug. 2025. URL: <https://cms.cern/> (visited on 09/07/2025).
- [9] *DELPHI*. Aug. 2025. URL: <http://home.cern/science/experiments/delphi> (visited on 09/07/2025).
- [10] D.E. Groom and S.R. Klein. “Passage of Particles Through Matter”. In: *Particle Data Group* (2020). Revised August 2019. URL: <https://pdg.lbl.gov/2020/reviews/rpp2020-rev-passage-particles-matter.pdf>.
- [11] *KEK To Kamioka*. Aug. 2025. URL: <https://neutrino.kek.jp/> (visited on 09/07/2025).
- [12] *L-Shell*. Aug. 2025. URL: <https://en.wikipedia.org/wiki/L-shell> (visited on 09/07/2025).

- [13] CSES Limadou. *CSES Limadou mission*. <https://www.cseslimadou.it/space-mission/>. Accessed: 2025-08-24. 2025.
- [14] CSES Limadou. *The CSES-01 mission*. <https://www.cseslimadou.it/cses01-satellite/>. Accessed: 2025-08-24. 2025.
- [15] CSES Limadou. *The CSES-01 mission*. <https://www.cseslimadou.it/cses02-china-seismo-electromagnetic-satellite/>. Accessed: 2025-08-24. 2025.
- [16] Nicolaidis Riccardo for the Limadou collaboration. *Time and energy resolved detection of gamma-ray transients with the High-Energy Particle Detectors onboard the CSES satellites*. July 2025. URL: <https://indico.cern.ch/event/1258933/contributions/6491286/attachments/3107185/5508164/ICRC25%20GRB%20HEPD-02-2.pdf> (visited on 08/30/2025).
- [17] P. Picozza et al. “Scientific Goals and In-orbit Performance of the High-energy Particle Detector on Board the CSES”. In: *The Astrophysical Journal Supplement Series* 243 (2019), pp. 16–32.
- [18] E. Ricci and on behalf of the LIMADOU Collaboration. “A pixel based tracker for the HEPD-02 detector”. In: *Proceedings of Science, 38th International Cosmic Ray Conference (ICRC2023)*. Vol. 444. Published online: August 17, 2023; Official publication: September 27, 2024. 2023, p. 164. DOI: 10.22323/1.444.0164.
- [19] Jakub Ripa. *Radiation Models (Udine, January 2020)*. https://agenda.infn.it/event/21252/contributions/108513/attachments/70149/87586/Udine_Jan_2020_Radiation_Models - Jakub_Ripa_v2.pdf. Accessed: 2025-08-24. 2020.
- [20] Cristian De Santis, Sergio Bruno Ricciarini, and on behalf of the CSES-Limadou Collaboration. “The High Energy Particle Detector (HEPD-02) for the second China Seismo-Electromagnetic Satellite (CSES-02)”. In: *Proceedings of 37th International Cosmic Ray Conference — PoS(ICRC2021)*. Vol. 395. Published online: July 07, 2021; Published in PoS: March 18, 2022. 2021, p. 058. DOI: 10.22323/1.395.0058.
- [21] Jonathan Shlomi, Peter Battaglia, and Jean-Roch Vlimant. “Graph Neural Networks in Particle Physics”. In: *arXiv preprint arXiv:2007.13681* (July 2020). arXiv: 2007.13681. URL: <https://arxiv.org/abs/2007.13681>.
- [22] *Spherical coordinate system*. Aug. 2025. URL: https://en.wikipedia.org/wiki/Spherical_coordinate_system (visited on 08/30/2025).
- [23] Space Environment Information System. *Earth's trapped particle environment, introduction and computational models*. <https://www.spenvis.oma.be/help/background/traprad/traprad.html#INTRO>. Accessed: 2025-08-24. 2018.
- [24] Martin. Walt. *Introduction to Geomagnetically Trapped Radiation*. Cambridge University Press, 2005.

- [25] R. L. Workman et al. “Review of Particle Physics”. In: *PTEP* 2022 (2022), p. 083C01.
DOI: 10.1093/ptep/ptac097.